

Melt segregation under compaction and shear channelling: Application to granitic magma segregation in a continental crust

Michel Rabinowicz¹ and Jean-Louis Vigneresse²

¹ UMR 5562, Observatoire Midi-Pyrénées, 14 Av. Edouard Belin, 31400 Toulouse, France

Michel.Rabinowicz@cnes.fr

² CREGU, UMR 7566 G2R, BP 23, 54501 Vandoeuvre, France

jean-louis.vigneresse@g2r.uhp-nancy.fr

Abstract

We present a model of melt segregation in a mush submitted to both compaction and shear. It applies to a granitic melt imbedded within a partially molten continental crust, able to sustain large stress values. The rheology of the melt and of the matrix constitute the external constraints. Time and length considerations also provide a posteriori constraints on the results. The mathematical derivation starts with the equations for melt and plastic flow in a mush. They are manipulated to obtain equations for the mean flow field and for the separation velocity. Assuming that the mean flow field is simple shear, a specific set of equations for the melt flow in a shear field is obtained. After simplifying the equations, they finally reduce to two systems of coupled equations. One is the well-known equation for compaction. The other is new and describes melt channelling during shear in a mush with a constant viscosity plastic matrix. Three free parameters are observed. One is the usual compaction length, and the two others are functions of the stress and strain amplitude during shear. Compaction instabilities lead to the development of spherical pockets rich in melt while shear channelling instability segregates melt in parallel veins. The size of the pockets and the distance between veins remain close to the compaction length. The two types of

instability segregate melt. But the compaction process is generally so sluggish that it cannot compete with the channelling one. The shape of the initial porosity perturbation has little influence on the final amplitude and wavelength of the generated structures. Scaling the equations provides insight on the dependence of the solutions on the initial parameters. Actually, the viscosity ratio between the matrix and its melt controls the compaction length, i.e. the distance that separates the main veins of segregated melts. The channelling time is controlled by the amount of inter-granular melt present in the system and of the amplitude of the shear stresses. During channelling the inter-granular melt is completely squeezed out from the volume in between veins. As melting progresses, the successive batches of melt, as well as the residual solid matrix, are increasingly more dehydrated. As a result, both phases progressively stiffen without changing their viscosity contrast and the associated compaction length. The segregation process stops when the dehydration process clamps the deformation of the solid matrix. Our model is surprisingly constrained to a narrow window of the parameters. This suggests that the compaction length L is metric or sub-metric, as is the distance between veins. Each channelling cycle leads to the segregation of a small amount of melt (about 5%) and lasts for about 30 ka to 300 ka. Those cycles are driven by the melting resulting from the heating due to diffusion of a deep heat source. The heat source must be located at some distance (about 10 km) from the melting zone, so segregation has time to develop as melting progresses. Few cycles may develop, but they restrict the amount of melt to about 20 % in total to be extracted from the matrix.

Abridged title	Granitic melt segregation						
Submitted to	Journal of Geophysical Research						
Version	19/11/03						
Pages	56	Words	15000	Characters	80000	Figures	7

First author's address Michel Rabinowicz

UMR 5562, Observatoire Midi-Pyrénées

14 Av. Edouard Belin

31400 Toulouse, France

Tel 335 6133 2962 Fax 335 6125 3202

mail michel.rabinowicz@cnes.fr

1. Introduction

Large amounts of magma result from enhanced melting joint with melt segregation. Whereas melting is controlled by the available heat, melt segregation is controlled by the external stress field. The source rock at the onset of melting has the appearance of a mush, a mixture of a weak phase within a stronger matrix. Melt segregates and migrates owing to a competition between compaction and channelling under shear. Compaction results from the buoyancy forces due to the difference of density between the melt and the solid grains. Melt channelling is induced by the stress gradient due to the plastic flow of the solid framework.

In the late 80's a mathematical formalism describing both melt compaction and channelling under shear of a mush emerged from several studies [Sleep, 1978; Scott and Stevenson, 1984; McKenzie, 1984, Stevenson, 1989]. Applications mostly considered melt migration within the mantle. Compaction spontaneously leads to melt concentration into spherical pockets [Scott and Stevenson, 1984; Richter and McKenzie, 1984; Scott and Stevenson, 1986; Wiggins and Spiegelman, 1995]. The melt pockets are soliton waves, called magmons [Scott and Stevenson, 1984] in Earth Sciences. They propagate as solitary waves, i.e. they can travel long distances without distortion [Drazin and Johnson, 1989].

Field data from ophiolite and lherzolite massifs partly support soliton development in the mantle [Ceuleneer and Rabinowicz, 1992; Ceuleneer et al., 1996; Rabinowicz et al., 2001; 2002]. Indeed, melt concentrates in the mantle owing to segregation under shearing at the interface between the lithosphere and the plastic mantle [Ceuleneer and Rabinowicz, 1992; Ceuleneer et al., 1996]. However, the relative scarcity of shear related impregnations proves that compaction dominates over channelling in the mantle in most cases. This can be explained by the weak amplitude of the stress gradient generated by mantle convection and/or plate drift compared to those of the melt buoyancy forces in the mantle.

Granitic magmas form in the intermediate to lower continental crust by dehydration melting of micas and/or amphiboles combined with quartz and plagioclases [Thompson, 1982; Clemens, 1990]. Biotite starts melting above a temperature of 800°C and the reaction is completed at 900°C [Patiño Douce and Johnston, 1991]. Melting requires additional heat, **for instance** provided by underplating mafic magmas from the mantle. At those temperatures, the continental crust is still able to sustain relatively high shear stress values in addition to a vertical load. Both stress systems should lead to competition between compaction and melt channelling by shear in case of a granitic mush. It represents a basic difference with melt segregation within mantle conditions.

Recent investigations on the rheology of partially molten rocks (PMR) point to non-linear feedback loops that interact during incipient melting [Vigneresse et al., 1996; Burg and Vigneresse, 2002]. They result from the large viscosity contrast, the random distribution of melt and the non linear amount of melt produced with increasing temperature. In addition, when the viscosity contrast becomes large enough, instabilities develop, leading to sudden jumps from the viscosity of the melt to that of the matrix, and the other way around [Vigneresse and Burg, 2003]. Discontinuous bursts of melt are expelled out of its matrix. Analogue and numerical models using a cellular automaton also document such irregular extraction of melt [Barraud et al., 2001; Bons et al., 2001; Vigneresse and Burg, 2000; Holtzman et al., 2003]. However the exact nature of such instabilities is not yet fully understood.

Direct applications of models derived from mantle conditions do not lead to expected discontinuities [Brown et al., 1995], nor to metric compaction length [McKenzie, 1984; Wiggins and Spiegelman, 1995] as observed **for granitic melts** in the field. Indeed, melt pockets are metric or sub-metric in size [Mehnert, 1968; Brown et al., 1999] as observed in migmatites (Figure 1). The time that leads to granite plutons formation is of the order of 1

Ma or less, as documented by isotopic ages or thermochronometry [Harayama, 1992; Harris et al., 2000]. We consequently consider a model that takes into account both compaction and shear in a strong continental crust with a weak molten phase. A careful manipulation of the equations reveals three possible driving terms for melt channelling during shear. The first one results from the softening of the viscosity of the solid matrix in presence of inter-granular melt films [Stevenson, 1989; Hirth and Kohlstedt, 1995]. The second results from interfacial stress gradients and damage [Ricard, et al., 2001]. At last, in the present article, we show that the proportionality of the deviatoric forces with the solid concentration causes channelling. This last effect is purely geometric and thus independent of the physical interaction between melt and solid. Being proportional to the amplitude of the shear stress, it is important only in case of a stiff mush submitted to large shear stresses as it is the case within granite bodies. As a consequence, this effect is systematically studied in the present paper. In the models, the scaling of the parameters allows direct variation and examination of their respective influence. The selected ones fit within constraints imposed by observations in granitic fields.

The article is organised as follows. In section 2, we discuss and adapt the equations governing melt motion within a deforming matrix. The whole system is submitted to vertical compaction and horizontal shear. In section 3, we fully detail the mathematical formalism. The basic equations of mass conservation and flow equations for the melt and the matrix describe compaction and melt channelling. When coupled, they form a set of dimensionless equations. This allows one to separately examine and resolve the horizontal melt migration triggered by the horizontal shear and the vertical migration due to compaction. In section 4, numerical results from 1D models describe melt redistribution due to shear instabilities. They are compared to 1D compaction models. In sections 5 and 6, we use the models to explain melt segregation in granite bodies.

2. Equations of state

We consider a mush composed of a highly viscous granular rock in which melt forms an interconnected network of tubes and surfaces at wetted grain boundaries. When subjected to stress, both the fluid and the solid phases flow, but strain preferentially partitions into the fluid. Two factors control the differential motion. The first factor results from the difference in pressure and the surface tension between the fluid and the solid. The second factor depends on the permeability of the matrix.

2.1 Rheology of the melt and its matrix

We consider partial melting in the continental crust under the action of a distant stationary source of heat. Granitic melts result from dehydration melting of muscovite and biotite [Thompson, 1982; Patiño Douce, 1999]. The former reaction starts above 700°C, but results in a smaller amount of melt, because of the restricted abundance of muscovite. We can neglect it in a first approach, though it does not provide enough melt to reach connection. The biotite breakdown reaction produces melt. It starts just above 800°C and is nearly completed at 900°C. A rough estimate is that 1% of melt should result from an increase of 1°C in temperature. The melt, which has a granitic composition, has a viscosity commonly ranging from 10^4 to 10^6 Pa.s, depending on its temperature, water content and degree of polymerisation when it starts cooling [Scaillet et al., 1997; Holtz et al., 1999]. It has a Newtonian viscosity, with a linear relationship between strain rate c_0 and stress σ . In contrast, the matrix has a power law dislocation creep rheology [Kirby and Kronenberg, 1987]:

$$c_0 = A \sigma^\gamma \exp(-Q/RT) \quad (1a)$$

In this expression, the exponential constant $\gamma = 3$, A is a pre-exponential constant (-11.2), Q an activation energy (150 kJ/mole) and R designates the Boltzmann constant. We adopt

experimentally derived values for quartz-bearing rocks [Kirby and Kronenberg, 1987; Wilks and Carter, 1990], at about 800°C because the melting conditions require those minerals to enter reactions. Hence, they also control rheology. Transforming the strain rate-stress relation into logarithmic coordinates yields a linear equation:

$$\text{Log } c_0 = 3 \text{ Log } \sigma - 26 \quad (1b)$$

in which the pre-exponential and the temperature-dependant terms are combined into the initial strain rate. In the same coordinates, and for comparison, the rheology of the melt reads, adopting an average viscosity of 10^5 Pa.s:

$$\text{Log } c_0 = \text{Log } \sigma - 5 \quad (1c)$$

However, crustal-derived melting is also the source of water exchange between the matrix and its melt. It influences the viscosity of both phases (Figure 2). At incipient melting, the melt presents its lowest viscosity (10^4 Pa.s) whereas the water content is the highest (about 5%) [Pichavant et al., 1992]. Conversely, when melting reaches about 50%, the water content stabilises at about 1% and viscosity is the highest at 10^6 Pa.s [Scaillet et al., 1997; Petford et al., 2000]. Simultaneously, the viscosity of the solid phase also varies. It decreases by about 3 orders of magnitude when temperature increases by 100°C to complete melting. The two effects modifies the viscosity, depending on the bulk percentage of melt. First, the mineral change in the solid phase strengthens it, replacing quartz and micas by plagioclase and sucking water. At present, there is no formal data on the strengthening of the crust under dehydration melting. We use an estimate derived from experimental deformation of wet and dry anorthite [Rybacki and Dresen, 2000], which considers only the strongest mineral, and thus provides an upper bound for crustal strengthening. The pre-exponential term (Equation 1) drastically decreases, whereas the activation energy increases by a factor of 3. We estimate that the viscosity of the solid phase linearly varies during melting as wet amphibolite is replaced by dry granulite. About 1% melting stiffens the crust by about a factor of 2 ($10^{0.33}$).

Therefore, 5 % melting stiffens the matrix by a factor of 32 ($10^{1.6}$), i.e. more than one order of magnitude. It is certainly an upper estimate for the stiffening of the matrix. Second, when the amount of melt is high (above 20-30%), the matrix partially loses its cohesion, and the mush behaves as a suspension [Lejeune and Richet, 1995; Vigneresse et al., 1996, Burg and Vigneresse, 2002]. The viscosity of the bulk material drops by more than about 10 orders of magnitude. Consequently, with ongoing melting, the melt and the matrix increase their viscosity in nearly the same proportion. This implies that their ratio does not change during melting.

2.2 Pressure

In a first approach, the resistance of the solid to deformation under isotropic stresses results from its bulk plastic viscosity [McKenzie, 1984]. However, this is not enough to account for the resistance to flow. Introducing the difference in pressure $\Delta P = P_m - P_f$ between both phases partly explains the differential flow [Scott and Stevenson, 1984; Bercovici et al., 2001a]. According to Bercovici et al., [2001a], such a difference, or “effective pressure”, relates to the rate of porosity change

$$\Delta P = -\frac{\mu_m}{\phi(1-\phi)} \frac{\bar{D}\phi}{Dt} \quad (2a)$$

in which μ_m is the instantaneous viscosity of the matrix and $\frac{\bar{D}\phi}{Dt}$ is the total derivative of melt concentration ϕ .

$$\frac{\bar{D}\phi}{Dt} = \frac{\partial\phi}{\partial t} + (\phi\mathbf{v}_f + (1-\phi)\mathbf{v}_m) \cdot \vec{\nabla}\phi \quad (2b)$$

where \mathbf{v}_m and \mathbf{v}_f designate the melt and solid velocities, and t is the time.

2.3 Surface tension and permeability

The surface tension S_T that develops between the two phases [Bercovici et al., 2001a] must also be estimated [Ricard et al., 2001]:

$$S_T = \bar{V}(\sigma\alpha) \quad (3)$$

where σ designates the reduced surface tension between the solid and liquid phases, and $\alpha \approx \frac{6\phi(1-\phi)}{d}$ is the variation of interfacial area per unit volume during deformation.

Melt migration and melt channelling essentially result from the non-linear relationship between porosity ϕ and permeability of the connected melt network $k(\phi)$. Laboratory experiments suggest that a mush with millimeter grain size and melt concentration of 1% has a permeability of 10^{-15} m^2 [Maaloe and Scheie, 1982]. A power law relationship between permeability and melt concentration ϕ is usually expected [McKenzie, 1984]

$$k(\phi) \propto d^2 \phi^n \quad (4)$$

where n is a dimensionless constant and d designates the characteristic size of the solid grains. The power law coefficient n depends on the topology of the melt network. A commonly used value is about 2 or 3 in the case of a flow confined to tubes and films, respectively. The geometry of the melt depends on the value of the dihedral angle of wetting. When the surface tension σ is small, the dihedral angle is also small ($20 - 30^\circ$) [Minarik and Watson, 1995]. In migmatites, a thin film of melt impregnates grain boundaries, leading to an interconnected network of melt [Mehnert et al., 1973; Brown et al., 1999; Swayer, 2001]. Conversely, at higher surface tension, the dihedral angle larger than 60° leads to restricted melt pockets stuck at grain triple junctions [Laporte and Provost, 2001].

Dihedral angles measurements in melts of granitic composition show that the surface tension between the two phases is large, but the angles remain smaller than 60° [Mehnert et al., 1973; Laporte, 1994]. Melts circulate within channels, yielding a power law coefficient close to 2. In static conditions, melt is connected only above a critical melt fraction ϕ_c and melt starts segregating only when porosity is larger. The threshold decreases in dynamic conditions and may even become almost negligible when strain acts on the mush [Vigneresse and Burg, 2003]. This implies that the melt content ϕ in the permeability law $k(\phi)$ (Equation 4) represents the excess of melt concentration. This value is the free parameter in our system. In what follows, the excess melt concentration is simply called melt concentration or mush porosity. It differs from the total melt percentage of the source $m(t)$. When successive cycles of melting and segregation develop, the melt percentage $m(t)$ is the sum of the ϕ of all cycles.

3. Mathematical formalism

3.1 Basic equations

The formulation developed involves the simultaneous solution of two sets of equations. They describe the vertical motion of the melt due to compaction and the horizontal motion due to shear. Both must be stated for the melt and the solid phase. For the sake of simplicity, these equations are finally non-dimensionalized. The governing equations to model two phase flows are: mass conservation, porous flow for the melt and plastic flow for its matrix. To this point our formulation is similar to previous work [Bercovici and Ricard, 2003].

Mass conservation for the melt and the solid

$$\frac{\partial \phi}{\partial t} + \vec{\nabla} \cdot (\phi \mathbf{v}_f) = 0 \quad (5a)$$

$$\frac{\partial(1-\phi)}{\partial t} + \vec{\nabla} \cdot ((1-\phi)\mathbf{v}_m) = 0 \quad (5b)$$

In Equations 5a and 5b, the density of both the fluid ρ_f and the solid ρ_m is assumed to be uniform, owing to the very small compressibility of both the melt and the solid (10^{-9} to 10^{-11} Pa⁻¹) [Agee and Walker, 1993].

Darcy equation

It expresses the stress balance that acts on the melt fraction ϕ of the porous media:

$$0 = \phi \left(-\vec{\nabla}(P_f + \rho_f g z) + \frac{\mu_f}{k(\phi)} \phi (\mathbf{v}_m - \mathbf{v}_f) \right) + \omega (\Delta P \vec{\nabla} \phi + \vec{\nabla}(\sigma \alpha)) \quad (5c)$$

with μ_f and ρ_f are the melt viscosity and density; g is the gravity acceleration and z is the vertical coordinate. The function ω designates the surface energy partitioning between the melt and the solid [Bercovici and Ricard, 2003]. The right hand side terms respectively designate the pressure gradient, the viscous stress gradient due to melt percolation, the stress gradient due to the pressure jump between the two phases ΔP , and finally the stress gradient due to the variation of the interfacial area during deformation.

Plastic flow equation

It controls the stress balance acting on the solid fraction $(1 - \phi)$ of the porous media

$$0 = -(1-\phi) \vec{\nabla}(P_m + \rho_m g z) + \vec{\nabla} \cdot ((1-\phi)\boldsymbol{\tau}_m) - \frac{\mu_f \phi^2}{k(\phi)} (\mathbf{v}_m - \mathbf{v}_f) + (1-\omega) (\Delta P \vec{\nabla} \phi + \vec{\nabla}(\sigma \alpha)) \quad (5d)$$

Here, ρ_m is the solid density and $\boldsymbol{\tau}_m$ the deviatoric stress tensor. The successive terms of the equation correspond to the effective pressure gradient in the solid, the viscous stress generated by the deformation of the solid, the stress due to the friction generated by melt percolation, the stress due to the pressure step between the solid and the liquid and the one due to surface tension.

The elastic stresses resulting from the compressibility of both the melt and the solid phases have been neglected. Indeed, they play a role during compaction only if the Deborah

numbers of either the fluid or the solid exceed unity [Sumita et al., 1996; Vasiliev et al., 1998, Fontaine et al., 2003]. The Deborah number is the product of the compressibility (about $<10^{-9} \text{ Pa}^{-1}$) by the amplitude of the deviatoric stress due to shear (about 10^7 Pa , see Table 1). Under such assumptions, the Deborah numbers for both phases are very small ($< 10^{-2}$) and may be neglected.

3.2 Equations for melt segregation and shear

We introduce the mean flow velocity field \mathbf{C} and the separation field \mathbf{S} :

$$\mathbf{C} = \phi \mathbf{v}_f + (1 - \phi) \mathbf{v}_m \quad (6a)$$

$$\mathbf{S} = \phi (\mathbf{v}_f - \mathbf{v}_m) \quad (6b)$$

Combined, both equations determine the differential velocity between the melt and its matrix

$$\mathbf{C} - \mathbf{S} = \mathbf{v}_m \quad (6c)$$

The respective densities of the solid and of the melt can be considered uniform, implying

$$\vec{\nabla} \cdot \mathbf{C} = 0 \quad (6d)$$

Hence, the Darcy equation (Equation 5c) becomes

$$\frac{\mu_f}{k(\phi)} \mathbf{S} = -\vec{\nabla} (P_f + \rho_f g z) + \frac{\omega}{\phi} (\Delta P \vec{\nabla} \phi + \vec{\nabla}(\sigma \alpha)) \quad (7a)$$

in which we decompose the first term as follows

$$-\vec{\nabla} (P_f + \rho_f g z) = -\vec{\nabla} (P_m + \rho_m g z) + (\vec{\nabla} \Delta P + \delta \rho \mathbf{g}) \quad (7b)$$

where $\delta \rho = \rho_m - \rho_f$ and \mathbf{g} is the gravity vector. We then use Equation 5d to estimate

$-(1 - \phi) \vec{\nabla} (P_m + \rho_m g z)$. It results that Equation 7a writes

$$\frac{\mu_f}{k(\phi)} \mathbf{S} = (1 - \phi) (\vec{\nabla} \Delta P + \delta \rho \mathbf{g}) - \vec{\nabla} ((1 - \phi) \tau_m) + \left(\frac{\omega}{\phi} - 1 \right) (\Delta P \vec{\nabla} \phi + \vec{\nabla}(\sigma \alpha)) \quad (7c)$$

The stress deviator verifies

$$\vec{\nabla} \cdot ((1 - \phi) \tau_m) = \vec{\nabla} \cdot ((1 - \phi) \mu_m (\vec{\nabla} \mathbf{v}_m + (\vec{\nabla} \mathbf{v}_m)^t)) - \vec{\nabla} \cdot \left(\frac{2}{3} (1 - \phi) \mu_m \vec{\nabla} \cdot \mathbf{v}_m \right) \quad (7d)$$

Considering Equation 6, together with Equations 2 to 7, we obtain the following set of equations:

Porosity

$$\frac{\partial \phi}{\partial t} + \vec{\nabla} \cdot ((1-\phi)\mathbf{S}) + \mathbf{C} \cdot \vec{\nabla} \phi = 0 \quad (8a)$$

Mean flow motion

$$\Delta P = -\frac{\mu_m}{\phi(1-\phi)} \left(\frac{\partial \phi}{\partial t} + \mathbf{C} \cdot \vec{\nabla} \phi \right) = -\frac{\mu_m}{\phi(1-\phi)} \vec{\nabla} \cdot ((1-\phi)\mathbf{S}) \quad (8b)$$

$$\vec{\nabla} \cdot \mathbf{C} = 0. \quad (8c)$$

$$\begin{aligned} & -(1-\phi) \vec{\nabla} (P_m + \rho_m g z) + \vec{\nabla} \times ((1-\phi)\boldsymbol{\mu}_m (\vec{\nabla} \mathbf{C} + (\vec{\nabla} \mathbf{C})^t)) = \\ & \vec{\nabla} \cdot ((1-\phi)\boldsymbol{\mu}_m (\vec{\nabla} \mathbf{S} + (\vec{\nabla} \mathbf{S})^t)) - \vec{\nabla} \cdot \left(\frac{2}{3} (1-\phi)\boldsymbol{\mu}_m \vec{\nabla} \cdot \mathbf{S} \right) - \frac{\mu_f \phi}{k(\phi)} \mathbf{S} - (1-\omega) (\Delta P \vec{\nabla} \phi + \vec{\nabla}(\sigma \alpha)) \end{aligned} \quad (8d)$$

Modified Darcy flow for the melt motion:

$$\begin{aligned} & \frac{\mu_f}{k(\phi)} \mathbf{S} - \vec{\nabla} \cdot ((1-\phi)\boldsymbol{\mu}_m (\vec{\nabla} \mathbf{S} + (\vec{\nabla} \mathbf{S})^t)) + \vec{\nabla} \cdot \left(\frac{2}{3} (1-\phi)\boldsymbol{\mu}_m \vec{\nabla} \cdot \mathbf{S} \right) = \\ & (1-\phi) (\vec{\nabla} \Delta P + \delta \rho \mathbf{g}) - \vec{\nabla} \cdot ((1-\phi)\boldsymbol{\mu}_m (\vec{\nabla} \mathbf{C} + (\vec{\nabla} \mathbf{C})^t)) + \left(\frac{\omega}{\phi} - 1 \right) (\Delta P \vec{\nabla} \phi + \vec{\nabla}(\sigma \alpha)) \end{aligned} \quad (8e)$$

The successive terms of the last equation (Equation 8e) relate the separation velocity \mathbf{S} to the effective pressure gradient, the buoyancy force, the gradient of deviatoric stresses induced by the mean flow field \mathbf{C} , and the surface stresses. Those equations (Equations 8a to 8e) constitute a complete set of coupled equations for ϕ , P_m , \mathbf{C} and \mathbf{S} . The surface energy partitioning function ω varies with melt concentration ϕ . Bercovici et al. [2001a] suggested that the surface stresses are equally balanced by the fluid and the solid. This hypothesis is verified when $\omega = \phi$. An alternative to this hypothesis is $\omega \approx 0$, because of the drastic contrast in viscosity between the melt and the solid [Bercovici and Ricard., 2003].

3.3 Equations for melt segregation within an uniform shear field

We assume that the mean flow \mathbf{C} results from the shearing movement along the fault. As long as the fluctuations of melt inside the fault are small, we can approximate \mathbf{C} by

$$\mathbf{C} = \begin{pmatrix} 0 \\ c_0 x \\ 0 \end{pmatrix} \quad (9a)$$

In the above expression, the coordinates x and y designate the horizontal coordinate normal and parallel to the fault axis, respectively (Figure 3). The parameter c_0 represents the shear induced strain rate of the solid framework (Equation 1b). Hence, c_0 relates to the shear velocity

$$c_0 = V/h \quad (9b)$$

in which h is the thickness of the shear zone and V its tangential velocity. In the present study, we are concerned with the early development of melt impregnation structures. Following Stevenson [1989], we assume that these structures result from the development of the separation field \mathbf{S} while at the same time the mean flow \mathbf{C} remains essentially unchanged. Consequently, in the following we assume that \mathbf{C} is independent of time and verifies Equation 9a. This hypothesis is likely verified as long as the generated melt impregnations have not been shifted along the plastic flow lines (see sections 5 and 6). Due to the shear, we rotate the two horizontal axis by 45° . The new coordinates X and Y correspond to the direction of maximum stretching σ_3 and maximum compression σ_1 respectively (Figure 3). The following expressions for the flow and stress fields are deduced

$$\mathbf{C} = \begin{pmatrix} \frac{1}{2}c_0(X-Y) \\ \frac{1}{2}c_0(X+Y) \\ 0 \end{pmatrix} \quad (9c)$$

$$\mu_m(\vec{\nabla}\mathbf{C} + (\vec{\nabla}\mathbf{C})^t) = \begin{pmatrix} \mu_m c_0 & 0 & 0 \\ 0 & -\mu_m c_0 & 0 \\ 0 & 0 & 0 \end{pmatrix} \quad (9d)$$

$$-\vec{\nabla} \cdot (1-\phi) \mu_m (\vec{\nabla} \mathbf{C} + (\vec{\nabla} \mathbf{C})^t) = \begin{pmatrix} \mu_m c_0 \frac{\partial \phi}{\partial X} \\ -\mu_m c_0 \frac{\partial \phi}{\partial Y} \\ 0 \end{pmatrix} \quad (9e)$$

To derive Equation 9e, we assume that μ_m is a constant. This is consistent with the assumption of a constant strain rate c_0 (see Equation 9b). Introducing Equation 9b into Equation 8d, we assume that ϕ is small, simplifying $(1 - \phi)$ to 1 and $\mu_m(1 + 1/\phi)$ to μ_m/ϕ . The simplified form for Equations 8a, 8b and 8d writes

$$\frac{\partial \phi}{\partial t} + \vec{\nabla} \cdot \mathbf{S} + \frac{1}{2} c_0 (X - Y) \left(\frac{\partial \phi}{\partial X} + \frac{\partial \phi}{\partial Y} \right) = 0 \quad (10a)$$

$$\Delta P = \frac{\mu_m}{\phi} \vec{\nabla} \cdot \mathbf{S} \quad (10b)$$

$$\frac{\mu_f}{k(\phi)} \mathbf{S} - \vec{\nabla} \cdot \left(\frac{\mu_m}{\phi} \vec{\nabla} \cdot \mathbf{S} \right) = \begin{pmatrix} \mu_m c_0 \frac{\partial \phi}{\partial X} + \left(\frac{\omega}{\phi} - 1 \right) \left(\frac{\partial(\sigma\alpha)}{\partial X} + \Delta P \vec{\nabla} \phi \right) \\ -\mu_m c_0 \frac{\partial \phi}{\partial Y} + \left(\frac{\omega}{\phi} - 1 \right) \left(\frac{\partial(\sigma\alpha)}{\partial Y} + \Delta P \vec{\nabla} \phi \right) \\ \delta \rho g + \left(\frac{\omega}{\phi} - 1 \right) \left(\frac{\partial(\sigma\alpha)}{\partial z} + \Delta P \vec{\nabla} \phi \right) \end{pmatrix} \quad (10c)$$

When ϕ is infinitesimal, the right-hand-side term of equation (10c), $\left(\frac{\omega}{\phi} - 1 \right) \Delta P \vec{\nabla} \phi$, is small in comparison with the left-hand-side term, $\vec{\nabla} \cdot \left(\frac{\mu_m}{\phi} \vec{\nabla} \cdot \mathbf{S} \right)$, because $\Delta P \vec{\nabla} \phi \approx \frac{\mu_m}{\phi} \vec{\nabla} \cdot \mathbf{S} \vec{\nabla} \phi$, see equation (10b), and $\vec{\nabla} \cdot \left(\frac{\mu_m}{\phi} \vec{\nabla} \cdot \mathbf{S} \right) \propto \frac{\mu_m}{\phi^2} \vec{\nabla} \cdot \mathbf{S} \vec{\nabla} \phi$. Hence, it is justified to drop the $\left(\frac{\omega}{\phi} - 1 \right) \Delta P \vec{\nabla} \phi$ term in equation (10c). This simplification is important, because it shows that the surface stresses triggered by the pressure difference between the solid and the liquid have no effect on the melt movement provided the melt concentration is infinitesimal. Moreover, it allows for the direct computation of \mathbf{S} based upon the melt distribution ϕ .

The three equations (10) form the core of our model. They respectively state the basic equation of melt conservation (Equation 10a), melt movement (Equation 10c), and effective melt pressure (Equation 10b). As shown in Bercovici and Ricard [2003], the equations of melt migration derived with Bercovici and Ricard [2003]’s formalism and with McKenzie [1984]’s formalism are similar provided: i) the melt concentration is infinitesimal, ii) the bulk viscosity of the mush introduced by McKenzie [1984] equals $\frac{\mu_m}{\phi}$. According to Scott and Stevenson [1984], the expression of the bulk viscosity is valid when the melt flows in cylindrical conduits. It applies to melt migration in granite because it occurs in intergranular channels (see section 2.2). These developments show that the modified Darcy flow equation (equation 10c) is independent of the surface stresses when they are equally balanced between the fluid and the solid, i.e. when $\omega=\phi$. This is clearly not the case, since the drastic contrast in viscosity between liquid and solid cancels ω .

The different possible formulations of solid and melt flow equations in a mush differ only by the terms describing the effects due to surface tension. In the present study, we assume that surface tension is negligible, which is an over-simplification. Bercovici et al. [2001b] derived the equations of melt migration during shear. Their method requires an explicit resolution of the coupling between melt segregation flow \mathbf{S} and shear flow \mathbf{C} , but it also takes into account the effects due to surface tension (Equation 8d), emphasising very important effects due to the surface tension generated during melt migration (see section 7). In the present study the model is based on a simplified but reasonable version of the flow equations.

To derive Equations 10, we use the same framework as Stevenson, [1989]. However, this author makes a distinct evaluation of the stress gradient generated by the shear movement $\bar{\nabla} \cdot (1-\phi)\mu_m(\bar{\nabla}\mathbf{C}+(\bar{\nabla}\mathbf{C})^t)$ compared to the one used in the present study. Because ϕ

is infinitesimal, Stevenson, [1989] assumes that $(1-\phi)\mu_m \approx \mu_m$, but considers that the matrix viscosity μ_m is not a constant but rather a function that depends on ϕ . This explains why the respective terms $\mu_m c_0 \frac{\partial \phi}{\partial X}$ and $-\mu_m c_0 \frac{\partial \phi}{\partial Y}$ are replaced, in the right hand side of the Darcy equation, by terms that are proportional to $\frac{\partial \mu_m}{\partial \phi} c_0 \frac{\partial \phi}{\partial X}$ and $-\frac{\partial \mu_m}{\partial \phi} c_0 \frac{\partial \phi}{\partial Y}$ (compared to our Equation 10c). The resulting equations are mathematically similar to ours. But they differ in their physical meaning. With our formalism, the segregation during shear results from the reduction of the resistive forces as the volume of the solid fraction decreases. Under Stevenson [1989]'s formulation, segregation is due to the softening of the matrix caused by the viscosity drop of increased interstitial melt fraction.

3.4 Simplified dimensionless equations for melt channelling and compaction

In the previous section, we have shown how to reduce the melt segregation problem to the resolution of a non-linear system that involves coupling between melt concentration ϕ and separation velocity \mathbf{S} (Equations 10). To nondimensionalize the equations, we choose scales for melt concentration, length, time, and consequently for velocity. The melt concentration ϕ inside the mush results from the balance between melting production and melt segregation. The mean inter-granular melt concentration during segregation ϕ_0 , noted here as the bulk melt concentration, is a quantity closely related to the coupling between segregation and melting. In case of melt segregation in the lower crust, ϕ_0 ranges from a few percent up to the critical rate for mush deconsolidation (around 20 %). In section 5, we show how to relate ϕ_0 to the heating rate of the crust and to the fault thickness h . From these remarks, it appears useful to scale the melt concentration ϕ by the bulk melt concentration ϕ_0 . The compaction length L is a good candidate to calibrate the lengths [Stevenson, 1989].

$$L = \sqrt{\frac{\mu_m k_0}{\mu_f \phi_0}} \quad (11a)$$

This considers the viscosity ratio between the matrix and the fluid, as well as the ratio between the mush permeability $k_0 = k(\phi_0)$ and the bulk melt concentration ϕ_0 . The scaling for the Darcy velocity v_d is

$$v_d = \frac{\delta \rho g k_0}{\mu_f} \quad (11b)$$

The scaling for time τ is

$$\tau = \frac{L \phi_0}{v_d}. \quad (11c)$$

The ratio v_d/ϕ_0 corresponds to the magma velocity during compaction inside the mush. τ is the time needed by the magma to move by a distance equal to the compaction length L .

Under such assumptions and scaling, Equations 10 become

$$\frac{\partial \phi}{\partial t} + \vec{\nabla} \cdot \mathbf{S} + N_v (X - Y) \left(\frac{\partial \phi}{\partial X} - \frac{\partial \phi}{\partial Y} \right) = 0 \quad (12a)$$

$$\Delta P = \frac{\vec{\nabla} \cdot \mathbf{S}}{\phi} \quad (12b)$$

$$\frac{1}{\phi^n} \mathbf{S} - \vec{\nabla} \left(\frac{1}{\phi} \vec{\nabla} \cdot \mathbf{S} \right) = \begin{pmatrix} N_s \frac{\partial \phi}{\partial X} \\ -N_s \frac{\partial \phi}{\partial Y} \\ 1 \end{pmatrix} \quad (12c)$$

in which two dimensionless numbers N_v and N_s are introduced. The first, N_v is the shear velocity divided by the compaction velocity. We call it the velocity number:

$$N_v = \frac{c_0 L \phi_0}{2 v_d}. \quad (13a)$$

In contrast, N_s is the ratio between the stress gradient and the buoyancy gradient. This expression is called the shear number:

$$N_s = \frac{\mu_m c_0 \phi_0}{L \delta \rho g} \quad (13b)$$

The set of Equations (12) allows us to compute the 3-D melt flow driven by shear and compaction. It is still too complicated to be resolved easily. To further simplify the problem,

we assume: (i) that $N_v(X-Y) \left(\frac{\partial \phi}{\partial X} - \frac{\partial \phi}{\partial Y} \right) = 0$, and (ii) that each X, Y and z component of the

separation velocity \mathbf{S} depends only on X, Y and z respectively: i.e. \mathbf{S} verifies:

$$\mathbf{S} = \begin{pmatrix} S_x(X) \\ S_y(Y) \\ S_z(z) \end{pmatrix} \quad (14)$$

The $N_v(X-Y) \left(\frac{\partial \phi}{\partial X} - \frac{\partial \phi}{\partial Y} \right)$ term represents the mass flow parallel to the fault plane transported

by the shear field \mathbf{C} : i.e. along the y-direction. The drop of this term in the equation (12a) can be justified if one assumes that the reference frame X, Y, z moves with the shear field \mathbf{C} (Figure 3). \mathbf{C} being not uniform along the x direction, the velocity of the reference frame should vary with x. In a geological context, see section 5, the horizontal separation of the melt during shear is small, and remains smaller than the compaction length L. Besides, the length h of the fault is large compared to the compaction length L. Hence, at the scale of the spot where melt channelling develops, the shear flow velocity C can be considered as locally uniform. It justifies that the melt redistribution at the compaction length scale can be studied

assuming an uniform shear, and thus assuming that $N_v(X-Y) \left(\frac{\partial \phi}{\partial X} - \frac{\partial \phi}{\partial Y} \right) = 0$. The shear

number N_v for the cases of geological interest is large: about 100. It results that the flow

velocity during shear is very large compared with the velocity at which melt is segregated. Accordingly, the melt impregnations themselves are strongly deformed by shear. This point is discussed in sections 5, 6 and 7.

We show in section 4 that the shear does not concentrate melt in the Y- direction, while in the X-direction melt spontaneously concentrates into several discrete places. Consequently, melt accumulates in planes parallel to Yz. Hence, the melt flow \mathbf{S} driven by the shear occurs only in the X-direction, and the one driven by compaction only in the vertical direction z.

To sum up, with the formalism used for melt compaction and shear melt channelling, two independent set of 1-D equations have to be resolved. The two sets are respectively called compaction and channelling equations. They write as follows:

i) A couple of scalar equations describes the vertical movement of the melt under compaction

$$\frac{\partial \phi}{\partial t} + \frac{\partial S_z}{\partial z} = 0 \quad (15a)$$

$$\frac{1}{\phi^2} S_z - \frac{\partial}{\partial z} \left(\frac{1}{\phi} \frac{\partial S_z}{\partial z} \right) = 1 \quad (15b)$$

They are similar to those found for 1D compaction in a mush with a small ($\phi \ll 1$) porosity [Scott and Stevenson, 1984; Wiggins and Spiegelman, 1995; Rabinowicz et al., 2002].

ii) A couple of equations describes the horizontal flow of melt induced by shear (melt channelling)

$$\frac{\partial \phi}{\partial t} + \frac{\partial S_x}{\partial X} = 0 \quad (16a)$$

$$\frac{1}{\phi^2} S_x - \frac{\partial}{\partial X} \left(\frac{1}{\phi} \frac{\partial S_x}{\partial X} \right) = N_s \frac{\partial \phi}{\partial X} \quad (16b)$$

Both sets of equations only differ by one term. The source term $N_s \frac{\partial \phi}{\partial X}$ on the right hand side of Equation 16b is replaced by a constant in Equation 15b. We call this term the ‘‘channelling

factor”. Scaling used to make the equations non-dimensional is the same for both the compaction and the channelling equations. Indeed, when the time scale τ (see Equation 11c) is divided by N_s , the new dimensionless channelling equations are not modified except that the source term of Equation 16b, $N_s \frac{\partial \phi}{\partial X}$ is also divided by the same value, leading to $\frac{\partial \phi}{\partial X}$. This means that the stress amplitude induced by shear accelerates the channelling process, but does not modify the spatial redistribution of melt during melt channelling. Accordingly, we can restrict the computation to the case of $N_s = 1$ (see next section).

4. Resolution of the coupled equations

As stated above, the formulation of the melt channelling under uniform shear introduced in this article is new, though aspects are very similar to Stevenson [1989]. We first present in section 4.1, a linear stability analysis of the channelling equations (Equations 16). In 4.2, solutions of the linearised version of the equations are compared to the full solutions of Equations 16. Because many studies present solutions of the compaction equations (Equations 15), we only present some typical solutions of these equations (see 4.3). They are later compared to those of the channelling equations.

4.1 Linear stability analysis of the channelling equations

We assume that instability develops when the porosity profile $\phi(X,t=0)$ departs from the value of 1 only by an infinitesimally small perturbation. Then as long as the variations of $\phi(X,t)$ remain small, we can assume that $\phi = 1$ in the left hand side of Equation 16b. Hence, the linear equations ruling the evolution of porosity verify

$$\frac{\partial \phi}{\partial t} + \frac{\partial S_x}{\partial X} = 0 \quad (17a)$$

$$S_x - \frac{\partial}{\partial X} \left(\frac{\partial S_x}{\partial X} \right) = N_s \frac{\partial \phi}{\partial X} \quad (17b)$$

The solutions of the linear set of Equations 17 are the superposition of sinusoidal functions with different waves numbers k . Therefore a mono-chromatic solution ϕ_k is represented by

$$\phi_k = 1 + \varepsilon_k(t) \sin(kX) \quad (18)$$

in which $\varepsilon_k(t)$ is given by

$$\varepsilon_k(t) = \varepsilon_0 \exp\left(N_s \frac{k^2}{1+k^2} t\right) \quad (19)$$

with ε_0 the initial amplitude of the periodic perturbation. It is inferred that, the melt distribution along the X-axis is linearly unstable. The growth rate of the periodic perturbation is $N_s k^2 / (1+k^2)$, which is equal to N_s for large values of k . Note that Stevenson [1989] found a similar dependence of the growth rates on the wave numbers k .

The linearised version of the melt channelling equations along the Y-direction verifies

$$S_Y - \frac{\partial}{\partial Y} \left(\frac{\partial S_Y}{\partial Y} \right) = -N_s \frac{\partial \phi}{\partial Y} \quad (20)$$

Therefore, the growth rate of any porosity perturbation along the Y-direction is negative and dampens with time. It demonstrates that melt channelling occurs only in the X-direction: the direction of maximum stretching σ_3 .

4.2 Numerical solutions of the channelling equations

The equations (Equations 16a, 16b) are solved in a periodic domain of length H . The channelling number N_s is chosen equal to 1. The finite difference method we use is based upon a second order scheme in time and a fourth order in space [Barcilon and Richter, 1986]. The region is discretized based upon a grid of 4000 points with a time step of 2×10^{-4} . The model starts with a porosity distribution that includes a small perturbation.

Reference model

We select a mono-chromatic porosity field ϕ_{k_0} to initiate a numerical solution to Equations 16. It verifies Equations 18 with the parameters $\varepsilon_0 = 0.2$, $k_0 = 2\pi/\lambda$, and the dimensionless wavelength $\lambda = 0.625$. The porosity waves are plotted at successive periods of time (Figure 4) over the domain of length $H = 2.5$. The model initiates at time $t = 0$, but soon, at time $t = 0.5$, instabilities develop with a relatively strong amplitude (± 0.34). However, their shape and amplitude look very similar to those computed using the linearised version of the melt channelling equations (Equations 17), both values being within 1%. From time 0.5 to 1.5, the growth rate of the instability remains very close to one. The maximal and minimal values of the perturbation stand at their initial position along the X axis. However, the bulk shape of the profile departs from a purely sinusoidal shape. The minimum values flatten, whereas their associated maximum becomes acute (Figure 4). At time 1.5, the amplitude of the porosity wave reaches 2.24 at its maximum and 0.38 at its minimum. Thereafter, the growth rate of the wave increases exponentially and leads to a runaway. Maximum values as 4.21, 8.22, 13.54, and 100 are reached at time 2, 2.25, 2.35 and 2.5 respectively. The corresponding minimum values decrease accordingly to 0.18, 0.09, 0.054, and 0.009 (Figure 4).

Preliminary conclusions

Instability develops in our reference model, leading to periodic porosity waves that exponentially increase in amplitude while they stretch in width (Figure 4). Conversely, porosity strongly decreases in between the spikes and shortly induces a complete drying out of the model. Such observations are consistent with the fact that melt migrates more easily when the porosity values are at their maximum. Therefore, when instability starts, it induces a feedback loop that increases porosity whereas melt extraction is facilitated. This reflects the influence of both the permeability, that varies as ϕ^2 , and the bulk viscosity of the mush, that

varies as ϕ^{-1} (see section 2). The sign of the right-hand side term $N_s \frac{\partial \phi}{\partial X}$, in Equations 16b or 17b, controls the direction of the separation velocity S_x . When negative, the melt moves downward. Alternatively, melt moves upward when the sign is positive. The change of sign explains melt accumulation close to the maxima and its drying out near the minima. Hence, between two successive minima of the initial porosity profile, all the melt that can freely migrate is expelled from the mush and is stored close to the maximum. In other words, when melt can percolate within the mush, it soon segregates into veins whose positions correspond to the maximum of the initial porosity profile. Since those veins are composed of 100 % of melt, their dimensionless width is $\lambda \phi_0$ and their spacing is λ .

Porosity-permeability dependence

To check the dependence between permeability and porosity (Equation 4) we run the same reference model assuming a cubic relationship instead of the square one. The runaway development is quite indistinguishable in both cases. It suggests that the variation of the effective viscosity of the mush with ϕ^{-1} in the left-hand-side of Equation 16b promotes and controls the development of the runaway. The variation of the effective viscosity of the mush with ϕ^{-1} also promotes the drastic amplification of the compaction waves (section 4.2) [Rabinowicz et al., 2002].

Amplitude and spacing of the initial instabilities

We run several cases to examine the evolution of the porosity wave when either its initial amplitude ε_0 or its wavelength λ is modified. With a smaller value of ε_0 , the onset of the non linear regime is delayed in time until the maximum amplitude of the wave fluctuation reaches 0.2, the initial amplitude before instabilities surge. Thereafter, the evolution of the wave mimics our reference model. This demonstrates that the development of the instability is insensitive to the initial amplitude of the wave. When halving or doubling the initial wavelength, the porosity profile is no more purely sinusoidal shape beyond time 0.5 while

the fluctuation of the wave exceeds ± 0.35 , the growth rate is still close to one up to time 1.5. Beyond that time, the runaway starts. For instance, at time 2, the maximum amplitude of the wave is equal to 4.27 and 3.95, respectively when the wavelength is halved or doubled. Nevertheless, both values remain close to the value of 4.21 observed for the initial wavelength λ_0 . As a consequence, the runaway process is synchronous for waves initiated with a sinusoidal profile with the same amplitude ε_0 and a wavelength λ of about one or less. When $\lambda = 5$ and $t \leq 1.5$, the growth rate of the wave (0.61) equals that of the linear regime. Beyond that time, the growth rate increases, leading to a runaway. However, the acceleration of the growth rate with time is much slower than that observed for an initial wavelength close to one. For instance, at time 2, the maximal amplitude of the wave is halved (2.11 instead of 4.21).

Initial shape of the instability

In our reference model, the initial instability is introduced through a sinusoidal perturbation (Equation 18). We already examined the wavelength dependence of the instability. We now focus on its bulk shape, and present tests run with a porosity profile ϕ with a very flat minimum (Figure 5). It verifies:

$$\phi = 1 + \frac{\varepsilon_0}{\cosh\left(A \sin\left(2\pi \frac{X}{H}\right)\right)} \quad (21)$$

where H denotes the length of the computational domain, $\varepsilon_0 = 0.2$ and A is a constant. The smaller are the values of A , the smoother the initial instability.

In a first set with smooth profile ($H = 5$ and $A = 4$ in Equation 21) the porosity profile initiates with two small maxima at a relative distance of 2.5. Instabilities develop in the vicinity of the local maximum of the initial perturbation (Figure 5a, b). Runaway starts after a time around 2. The triggered transient melt flow induces a nearly uniform depletion of melt in the region between the instability spikes. In the second test, the spikes of the initial

perturbation are strongly reinforced ($H = 50$ and $A = 40$). Two local maxima develop at a respective distance of 25 but the instability absorbs melt only over a distance comparable to the width of the peak of the initial porosity profile (Figure 5c).

A complete drying out of melt between the two spikes results from the superposition of two highly non-linear instabilities. The first instability expels all the melt from the region close to the local minima. The second concentrates the available melt toward the region of the local maxima of the initial porosity profile. The two instabilities have an different cause, but cooperate to concentrate melt.

Competition between instabilities with different wavelength

The linear stability analysis does not allow to determine the characteristic distance λ of the dikes generated during melt channelling. As long as the amplitude of the waves remains small, the linear-instability-regime prevails. All wavelengths with $\lambda \in [0, 1]$ develop with the same growth rate. During the runaway development, the growth rate of the instabilities with a small λ is similar to that with $\lambda \approx 1$, but a bit faster. We show below the predominance of the instability with a wavelength close to 1 during the runaway.

To control the predominance of such a wavelength, we tested models in which the initial porosity profile ϕ is the superposition of two sinusoidal functions with the same amplitude ε_0 but with a different wavelength, with $\lambda_1 > \lambda_2$. In this test case, ϕ verifies

$$\phi = 1 + \varepsilon_0 \left(\sin\left(\frac{2\pi}{\lambda_1}(X-a)\right) + \sin\left(\frac{2\pi}{\lambda_2}X\right) \right) \quad (22)$$

in which a phase-shift a is introduced to prevent tuning. We use the values of $\varepsilon_0 = 0.1$ and $a = 0.1$ as initial instability parameters. We test four different wavelet couples: $\lambda_1 = 5$ and $\lambda_2 = 0.625$, $\lambda_1 = 2.5$ and $\lambda_2 = 0.625$, $\lambda_1 = 1.25$ and $\lambda_2 = 0.625$, $\lambda_1 = 0.625$ and $\lambda_2 = 0.3125$. Snapshots of melt channelling experiments at time $t = 2$ are displayed in Figure 6. They

allow for direct comparison with the reference model (Figure 4), and in between them (Figure 6a to 6d).

In a first run (Figure 6a), the two wavelengths are significantly different, ($\lambda_1 / \lambda_2 = 8$). The runaway development associated with the $\lambda_1 = 5$ wavelet is delayed in time. During the delay, the available melt is dried up by the exponentially growing wavelets associated to λ_2 . When the two superimposed instabilities have similar wavelengths (λ_1 / λ_2 close to 1), melt runs out only from the instability associated to λ_2 (Figures 6b, 6c and 6d). The associated spikes are damped, while the remaining ones collect a large volume of melt from their neighbourhood. The characteristic spacing of the generated veins is close to λ_1 , and their thickness is $\lambda_1\phi_0$. This corresponds to the spacing and thickness associated with the largest wavelength. Although the development of the runaway associated to λ_2 is delayed in time, it still occurs. But, during the time lag, a large volume of melt has already been stored into veins of λ_1 -type. It is thus expected that λ_2 -type veins are very thin: i.e. they have a thickness representing only a fraction of $\lambda_2\phi_0$.

To summarize, an instability with a large wavelength (e.g. $\lambda = 5$) should never develop in competition with a wavelength close to 1 because its growth rate is too small. Conversely, the development of a λ_2 -type instability is inhibited (Figures 6b-d, in which λ_2 is less than 1) because the instability associated with λ close to 1 absorbs the largest amount of melt. Therefore melt channelling distributes melt in veins with a characteristic distance close to 1 and thickness of about ϕ_0 (Figure 3). Indeed, their distribution is certainly very irregular because of the development of numerous thin and closely-packet vertical veins (as in models of Figures 6). The time needed to generate the major veins depends on the amplitude of the initial perturbation ε_0 . When its amplitude is large, i.e. $\varepsilon_0 = 0.2$, a delay in time of 2.5 is necessary to reach runaway (Figure 4). Because of the growth rate of 1 of the instability

during the period of linear growth of the wave (Equation 19), a time delay of 6 is expected to reach the runaway provided $c_0 = 6 \cdot 10^{-3}$. The perturbation that is expected to trigger the instability results from local viscosity and permeability variations due to fluctuations of the melting rate, grain size distribution, and mineralogy of the solid phase. Henceforth, the “noise” during melt channelling is probably strong. This leads us to suggest that a lapse of time of 6 before reaching runaway is probably a maximum estimate.

4.3 Solutions of the compaction equations

This part of the process has already been investigated by several authors [McKenzie, 1984; Scott and Stevenson, 1984; Ricard et al., 2001; Wiggins and Spiegelman, 1995; Rabinowicz et al., 2001 and 2002]. Consequently, we do not examine it in details, but in relation with the preceding melt channelling process. We focus on the effects compaction has on melt motion.

The $N_s \frac{\partial \phi}{\partial X}$ term, at the right hand side of Equations 16b or 18b has a predominant role (see section 4.2). Its sign controls the motion of the melt, which is upward when the term is positive and downward when the term is negative. Melt motion stops when this term becomes null. In the compaction equations (Equations 15), this term is always equal to 1. This signifies that melt is always pushed upward by the buoyancy forces. In contrast, the melt motion slows down when $\frac{\partial \phi}{\partial z} < 0$ [Wiggins and Spiegelman, 1995]. This term is included in the left hand side of Equation 15b, owing to the power law permeability versus porosity dependence (Equation 4). Therefore, when the initial porosity is a decreasing function of z , the porosity field splits into discrete waves in which melt concentrates. In the case of a granitic mush, the decrease of porosity with z that triggers the development of waves can result from melt crystallisation in the upper levels of the crust.

We study a possible stopping of the melt motion (“obstruction”) by examining the relative decrease in porosity values. We label obstruction as weak when the upward drop in porosity is less than 5. Conversely, it becomes drastic when the drop ranges from 100 to 1000. This requires testing the instability model for a long period of time. We tested both cases of weak and drastic obstruction with snapshots at time 50 (Figure 7). The initial porosity profile F_{in} verifies:

$$F_{in}(z)=1 \quad (23a)$$

otherwise

$$F(z)=\frac{(1-c_{\infty})}{\cosh(0.5(z-25))}+c_{\infty} \quad (23b)$$

Testing for obstruction, the asymptotic concentration c_{∞} is adjusted to 0.5 and to 0.001 respectively for the weak and drastic cases. We solve the compaction equations (Equations 15) based upon the same numerical method as for melt channelling (section 4.2). Since gravity forces push the melt upward, there is no stationary solution to the compaction equations. Accordingly, we assume that melt freely migrates to the top and to the bottom of the integration domain: i.e. $\frac{\partial \phi}{\partial z} = \frac{\partial S_z}{\partial z} = 0$ at those points.

In case of a weak obstruction, the melt concentrates at the top of the wave train, as expected. However, saturation occurs at a value exceeding ϕ_0 by a few times the porosity drop of the initial porosity profile $(1-c_{\infty})\phi_0$, (see Figure 7a). The dimensionless width of the impregnated domain is about 5, and the background melt concentration just exceeds $c_{\infty}\phi_0$. Conversely, in case of drastic obstruction, saturation occurs for a concentration a few ten times the bulk porosity ϕ_0 (Figure 7b). The dimensionless width of the impregnated domain is about 1, and the background melt concentration becomes negligible. The dimensionless time to reach the asymptotic regime during compaction is about 50, i.e. an order of magnitude larger than that needed to develop veins during shear, at most a dimensionless

time of 6 though we assume that $N_s = 1$. The dimensional time needed to squeeze melt into veins under shear is $\tau_s \approx 6\tau/N_s$, whereas the time to generate solitons by compaction is $\tau_c \approx 50\tau$. The thickness of the impregnated domain ranges between L and $5 \times L$, whereas the thickness of the veins is equal to $\phi_0 L$. Compaction perfectly separates the melt free to percolate from its solid matrix only when the initial obstruction is drastic. This is always the case during melt channelling. Melt pockets generated during compaction migrate upward, pushed by the buoyancy forces, while the melt channelling process rapidly leads to a static asymptotic regime in which the liquid and solid phases are completely separated.

5. Conditions for instability development

Sections 3 and 4 display equations and models observed in the general context of geological problems. In the present section, we restrict their application to granitic melt segregation in the continental crust. We proceed in four steps: i) we estimate the ranges of values for the different parameters, ii) we derive precise scaling laws for the different variables, iii) we analyse different scenarii for melt segregation in the lower crust, and finally iv) we constrain the transient evolution of the plastic shear zone in a fault.

5.1 Parameter values for melt segregation in the lower crust

Our model uses non-dimensional parameters for length and time (Equations 11 to 16). Because they are scaled with respect to the other parameters (μ_f , μ_m , ϕ_0 , k_0 , h , g , V , $m(t)$, and $\delta\rho$), we examine their variations as the initial values are modified. We first examine the range of all values as they are introduced in the model. Some are fixed, given in textbooks. Some vary within a limited range, the cause of variations being known to vary with time during melting $m(t)$ and segregation.

Fixed parameters include the gravity constant ($g = 10 \text{ m}^2/\text{s}$), the density contrast between the solid and the melt ($\delta\rho = 400 \text{ kg/m}^3$), the shear velocity on the fault ($V \approx 3\text{cm/yr}$) and the permeability of the mush, according to millimeter grain size and 1% of interstitial melt ($k_0 = 10^{-15} \text{ m}^2$) [Maaloe and Scheie, 1982; McKenzie, 1984]. Variable parameters include the matrix and fluid viscosities μ_m and μ_f , which increase with decreasing water content (section 2.1 and Figure 2), the bulk melt concentration ϕ_0 , the melting rate $m(t)$ and the width of the fault h .

The shear zone width of major fractures in the Earth is pluri-kilometric [Leloup et al., 2001]. It does not mean that the plastic flow in the deep crust occurs simultaneously along the entire width of the shear zone. More likely, the deformation integrates a swarm of plastic deformation events confined in quasi-vertical slots whose thickness h represents a small fraction of that of the shear zone. If the seismologically active fields in the upper crust are described as very localised objects often with a metric thickness, it is expected that the plastic deformation slots at the deep crust have a thickness h of about 100 m [Scholz, 1990]. Besides, as shown below, shear and melt segregation progressively reduce the thickness of the plastic shear zone h with time: hence $h=h(t)$ depends on time t . Consequently, we consider h as a free parameter ranging in a 10 m to 10 km interval.

The fault activity controls the successive pulses of magma that make a granite pluton. Internal chemical variations, discordant fabrics document the successive bursts of magma. Isotopic data presently fails to adequately separate the internal time span between successive bursts. However, discordant temperatures determined from zircon and monazite thermometry document that melt might have been extracted in less than 10 ka for the Himalayan granites [Harris et al., 2000]. Several considerations about ascent velocity and freezing conditions also bracket the emplacement to less than 100 ka [Petford et al., 2000]. These numbers can be used to derive reasonable ranges for the time of generation of veins by

shear channelling $\tau_s \approx 6\tau/N_s$ or melt pockets by compaction $\tau_c \approx 50\tau$ (see section 4). We assume that the discharge during one magma burst results from one segregation sequence. Accordingly, each burst is characterized by the bulk melt concentration ϕ_0 and the effective thickness h of the active portion of the fault. As a consequence, the segregation sequence is also a function of the melting rate $m(t)$. When melting starts, $\phi_0(t)$ is equal to $m(t)$. Nevertheless, $\phi_0(t)$ differs from $m(t)$ after the first segregation loop. To summarize, **granitic** melt segregation depends on three free parameters h , ϕ_0 and m that all evolve with time (see below and section 6).

5.2 Scaling laws for melt segregation in granites

In order to determine different scenarii for melt segregation in granites (section 5.3), we use a reference set of parameter values for scaling (denoted by the indices sc) and then display the functions relating the different variables to h , ϕ_0 and m . In this reference set, the shear zone width is $h_{sc} = 100\text{m}$, the bulk melt concentration $\phi_{sc} = 1\%$, and the strain rate $c_{sc} = V/h_{sc} = 3 \text{ cm.s}^{-1}/100 \text{ m} \approx 10^{-11} \text{ s}^{-1}$. The melt viscosity is fixed at $\mu_{sc}^f = 10^4 \text{ Pa.s}$, corresponding to a water content of about 1% (see Figure 2). The matrix viscosity is $\mu_{sc}^m = 10^{16} \text{ Pa.s}$, corresponding to an hydrated matrix under a strain rate c_{sc} of 10^{-11} s^{-1} and a temperature of 800°C (see section 2.1). This implies a deviatoric stress scale $\sigma_{sc} = \mu_{sc}^m c_{sc}$ of 0.1 MPa .

Compaction length

The compaction length is a key variable in our problem (Equation 11a). It determines the characteristic distance between the main veins and the size of the compaction pockets. It can be expressed as

$$L(h, \phi_0, m) = L_{sc} \left(\frac{\mu_f(m)}{\mu_{sc}^f} \right)^{-\frac{1}{2}} \left(\frac{\mu_m(m, C_{sc})}{\mu_{sc}^m} \right)^{\frac{1}{2}} \left(\frac{\phi_0}{\phi_{sc}} \right)^{\frac{1}{2}} \left(\frac{h}{h_{sc}} \right)^{\frac{1}{3}} \quad (24)$$

where $L_{sc} = .3$ m.

Channelling number

A suitable combination of Equations 11 and 13b shows that the channelling number verifies

$$N_s(h, \phi_0, m) = N_{sc}^{sc} \left(\frac{\mu_f(m)}{\mu_{sc}^f} \right)^{\frac{1}{2}} \left(\frac{\mu_m(m, C_{sc})}{\mu_{sc}^m} \right)^{\frac{1}{2}} \left(\frac{\phi_0}{\phi_{sc}} \right)^{\frac{1}{2}} \left(\frac{h}{h_{sc}} \right)^{-\frac{2}{3}} \quad (25)$$

where $N_{sc}^{sc} = 1$

Velocity number.

It verifies (Equations 11 and 13a)

$$N_v(h, \phi_0, m) = N_{sc}^{sc} \left(\frac{\mu_f(m)}{\mu_{sc}^f} \right)^{\frac{1}{2}} \left(\frac{\mu_m(m, C_{sc})}{\mu_{sc}^m} \right)^{\frac{1}{2}} \left(\frac{\phi_0}{\phi_{sc}} \right)^{-\frac{1}{2}} \left(\frac{h}{h_{sc}} \right)^{-\frac{2}{3}} \quad (26)$$

where $N_{sc}^{sc} = 37$.

Time.

The times needed to generate veins by shear channelling $\tau_s \approx 6\tau/N_s$ and to generate melt pockets by compaction $\tau_c \approx 50\tau$ result from the manipulation of Equations 11 and 25:

$$\tau_s(h, \phi_0) = \tau_{sc}^{sc} \left(\frac{\phi_0}{\phi_{sc}} \right)^{-1} \left(\frac{h}{h_{sc}} \right) \quad (27)$$

$$\tau_c(h, \phi_0, m) = \tau_{sc}^{sc} \left(\frac{\mu_f(m)}{\mu_{sc}^f} \right)^{\frac{1}{2}} \left(\frac{\mu_m(m, C_{sc})}{\mu_{sc}^m} \right)^{\frac{1}{2}} \left(\frac{\phi_0}{\phi_{sc}} \right)^{-\frac{1}{2}} \left(\frac{h}{h_{sc}} \right)^{\frac{1}{3}} \quad (28)$$

where $\tau_{sc}^{sc} = 1.5$ Ma and $\tau_c^{sc} = 12.5$ Ma. **In the** above expressions, **time** to generate veins by shear $\tau_s(h, \phi_0)$ is independent on the viscosity of both the melt and the solid. From Equations 27, 28, we deduce that $\tau_s \ll \tau_c$, for most of the reasonable parameter values of h , ϕ_0 and m

(see Table 1). It is thus expected that melt channelling is generally the dominant mode of melt segregation in the continental crust. Consequently, veins with a characteristic spacing of L and a thickness of $L\phi_0$ should be generated inside σ_1 -planes.

Shear strain.

The displacement of each fault edge δl during the vein generation τ_s equals:

$$\delta l(h, \phi_0) = 6 \frac{N_v}{N_s} h = 220 \left(\frac{\phi_0}{\phi_{sc}} \right)^{-1} h \quad (29)$$

This expression is independent on the viscosity of both the solid and the melt. Its value is always greater than h , which is itself much greater than L (see Table 1). Consequently, the horizontal displacement of the mush is much **larger** than that of the matrix. The horizontal motion of the melt is the superposition of the flow during channelling and the shear flow C (Equation 9a). The vertical veins trend along the direction of maximum compression during shear (section 4.1). Those planes rotate under the shear field C and progressively take a S-shape (Figure 3). In particular, those S-shape surfaces become parallel to the shear direction, approaching the edges of the shear zone. When deformation localises into such planes, it favours melt channelling, but also decreases the effective pressure inside the mush (Equation 10b), damping the melt channelling process. This suggests that melt channelling acts as a stop and go process.

Shear Stress.

Because water content decreases with total melting m , the viscosity of the matrix μ_m is a function of both the melting m and the constant applied strain rate $c_0 = V/h$ during shear (Equation 9b). Its value increases by about one order of magnitude when melting increases by about 5%. As a consequence, the stiffness of the matrix increases accordingly. The stress level SH required to initiate fractures writes:

$$SH(h, m) = \sigma_{sc} \left(\frac{h}{h_{sc}} \right)^{\frac{1}{3}} \times 10^{\left(\frac{m}{5\phi_{sc}} - 1 \right)} \geq 40 \text{ MPa} \quad (30)$$

For instance when $h = 100 \text{ m}$, a maximum of 20% of melt can segregate before the mush becomes too stiff to be deformable, and thus become brittle (see Table 1 and section 5.3)

5.3 Various scenarii for melt segregation in a partially molten region of the crust

Though melting is relatively constrained, continuous melting requires a heat source that could keep the source zone able to generate more melt after a first burst of melt has been segregated. This **point** addresses melt evolution with time $m(t)$. It depends on heat transport between a deeper hot intrusion and the melting region. We assume that heat is transported by conduction over the distance D , resulting in a scaling of the melt variation with time $\delta m(t)/\delta t = \kappa/D^2$, in which κ is the thermal diffusivity ($10^{-6} \text{ m}^2\text{s}^{-1}$). Full melting is reached within a time D^2/κ , and partial melting to ϕ reached in $t_\phi = \phi D^2/\kappa$.

Melting and segregation are synchronous. As bulk melt concentration ϕ_0 increases in the mush with melting, a fraction of it segregates, establishing a balance between the rate of melting and the rate of segregation. A stationary inter-granular melt concentration during shear ϕ_0 is reached when both rates are identical. From a physical point of view, it seems that the time needed to produce a ϕ_0 quantity of melt fraction equals the time $\tau_s(h, \phi_0)$ required to segregate the same melt fraction. Hence, using Equation 27 and the scaling value $\sqrt{\kappa\tau_s^{sc}\phi_{sc}} = 670 \text{ m}$, we find:

$$\phi_0(h, D) = \frac{\sqrt{\kappa\tau_s^{sc}\phi_{sc}}}{D} \left(\frac{h}{h_{sc}} \right)^{\frac{1}{2}} \quad (31a)$$

This expression allows us to relate the bulk melt concentration ϕ_0 to a couple of geometrical parameters: the thickness h of the shear zone and its distance to the heat source D . As a

consequence, the whole problem of melt migration under shear depends on three parameters with clear geological meaning: $h(t)$, $D(t)$, and $m(t)$.

Three distinct situations should be **separately considered** : i) the heat source is so close to the lower crust interface that the bulk melt concentration ϕ_0 exceeds 20%; ii) **the heat source** is far enough so that the heating rate is low and the bulk melt concentration ϕ_0 is low, about 1%. iii) the heat source favours development of a mush with a bulk melt concentration ϕ_0 of about 5 % to 10% (Table 1).

High melting conditions – heat source close to the segregation zone

According to Equation 31a, the bulk melt concentration ϕ_0 exceeds 20% when the heating source is located at a distance D beneath the lower crust that verifies:

$$D < 2.15 \text{ km} \times \left(\frac{h}{h_{sc}} \right)^{\frac{1}{2}}. \quad (31b)$$

Melting is fast and leads progressively to matrix de-cohesion [Vigneresse et al., 1996]. In several steps, the viscosity of the matrix viscosity drops by more than 10 orders of magnitude. Each step reduces, by two or three orders of magnitude, the compaction length $L(h, \phi_0, m)$ and the compaction time τ_c (Equations 24, 28). The corresponding compaction length L ranges from mm to few cm. The time needed to generate melt pockets by compaction τ_c decreases accordingly. It becomes lower than the melt channelling time τ_s since the later is invariant with the matrix viscosity (Equation 27). Therefore, melt compaction becomes faster than melt channelling. The growth rate of the melt pockets is proportional to the amplitude of the initial porosity “obstruction” (section 4, Equation 23). Melt pockets are small, owing to the small compaction length, except in a very narrow boundary layer. Thus, compaction concentrates only a very small volume of melt. Accordingly, shear channelling localises the essential amount of melt to produce thin veins

spaced from mm to cm. Eventually, close to the boundary layer, melt pockets as wide as $5 \times L$ are generated. Besides, the matrix viscosity softening during deconsolidation is known to modify compaction [Rabinowicz et al., 2001], and channelling [Stevenson, 1989]. These studies show that the intergranular melt volume in excess of the critical rate for deconsolidation flows in pockets or veins. As a consequence, flow stops when the interstitial melt volume equals the critical rate.

Very slow melting conditions

When both the melting rate $m(t)$ and the bulk melt concentration ϕ_0 are around 1%, the compaction length L increases from about 15 cm to up to 3 m as the thickness of the shear zone h varies from 0.01 to 10 km (Equation 24). The time required for compaction increases from 5.8 to 58 Ma and is comparable to the time for shear channelling that ranges 0.15 to 150 Ma. (Equations 27 and 28). These numbers attest that channelling is the dominant mode of melt segregation for a shear zone about 1 km in width. But the time required, even for melt channelling, is large compared to observations. It rules out efficient melt segregation when melting is slow.

Moderate melting conditions

We now consider segregation acting on a moderate bulk melt concentration: ϕ_0 about 5-10% (see cases illustrated in Table 1). The situation corresponds to a source in the temperature range of 810-820 °C. The heating source is distant from 2 to 40 km and the shear zone width h varies from 10 m to 10 km interval (Equation 31). Compaction length decreases in size compared to low melting conditions (Equation 24). It ranges from 0.33 m to 3.5 m provided the shear zone varies from 0.01 to 10 km in thickness. The time necessary for segregation under shear channelling reduces to 30 ka for a 10 m thick shear zone and to 15 Ma for the extreme case of a 10 km thick shear zone. Compaction time is still larger than shear channelling, competition now develops between melt segregation and melt production.

Several successive cycles of melting and segregation may develop. However, a supplementary constraint operates, owing to the increase in strength of the matrix when magma is extracted. One consequence of melt extraction is that it leaves dehydrated minerals in the source zone, stiffening the source rocks. However, the parallel evolution of the matrix and melt viscosity leaves the shear channelling conditions unchanged (Equation 27). The stress amplitude increases with ongoing melting (SH in table 1). It soon becomes close to the yield for mechanical rupture: about 40 MPa [Renner et al., 2000], which limits the number of successive cycles to be achieved (Equation 30).

We examine four situations with different couples of values D and h . According to Equation 31a, three couples lead for each cycle of segregation to a bulk melt concentration ϕ_0 of 5%: ($D = 2.7$ km, $h = .01$ km), ($D = 8.7$ km, $h = .1$ km) and ($D = 27$ km, $h = 1$ km). The last couple ($D = 43$ km, $h = 10$ km) leads to a bulk concentration ϕ_0 of 10 %.

When the distance to the heat source is relatively large ($D = 43$ km), with a thick shear zone ($h = 10$ km), channelling and compaction develop during the first cycle of melting. Both compaction and segregation times are similar, though they remain shorter than the time for heat to diffuse and to warm the source region. Compaction time increases by one order of magnitude after the first cycle. We therefore suggest that compaction does not stay any longer competitive. When $m = 30\%$ is completed, that is after about 3 cycles, the shear stress is 10 MPa, still well below the possible yield for fracturing (40 MPa) [Renner et al., 2000]. This value is computed using the matrix viscosity value at 800°C, but it drops by about a factor of 6 if temperature is changed to 830°C (section 2). When taking into account this viscosity drop, the shear stress may be as low as 1.5 MPa. Thus 40 % of melt can segregate during a last segregation cycle. However, the total time required for extracting this volume of melt is 4×15 Ma = 60 Ma. Obviously this value is inconsistent with observed time data.

In case of smaller values for the two distances ($D = 27$ km; $h = 1$ km), four segregation cycles may develop, yielding a total melting $m = 20\%$. The shear stress amplitude after four cycles is 46 MPa. However, this value is computed using the viscosity value at 800°C . When changed to 815°C , it drops by a factor of about 2.5 (section 2), resulting in a shear stress well within the yield for mechanical rupture. The time needed to complete the four cycles reduces to about 12 Ma, which is an upper limit for generating magmas.

In situations where the shear zone is thin ($h = 0.1$ km) and at moderate distance from the heat source ($D = 8.7$ km), complete melting is achieved in about $D^2/\kappa = 2.5$ Ma. A melting increment of 5% requires only 0.3 Ma. Several sequences of melt segregation can develop. Compaction time takes 20 times longer than in the case of shear channelling, even during the first compaction cycle. Only vertical veins can be generated. They are spaced by compaction length (0.7 m) and they thicken by about 3.5 cm after each channelling sequence. Owing to melting and water exchange between the solid and liquid phases, their respective viscosity drops by one order of magnitude at the end of the first segregation event. Hence, the compaction length remains invariant, but the effective deviatoric stress equals 0.1 MPa. Therefore at the end of the third segregation cycle, the shear stress level is 100 MPa and mush becomes stiff enough to reach mechanical rupture. Taking into account the viscosity drop for temperature, i.e. 2.5 orders of magnitude (see above), a total of about four cycles of segregation is possible. They would take about 1.2 Ma to develop, leading to a total melt segregation of 20%.

When the shear zone is thin ($h = .01$ km), the compaction length reduces accordingly to about 0.33 m. It induces also a much shorter time for melt segregation (30 ka). This compares well with the 10 ka time of extraction of the melt in Himalayan granites (see 5.2). The total time for several cycles of melting remains large in comparison to the time of

heating of the mush by a source located at 2.15 km (160 ka). Taking into account of the viscosity drop due to temperature increase from 800°C to 815°C, the shear stress SH after three channelling sequences is about 100 MPa, indicating that a fourth cycle cannot be entirely completed before fracturing. Hence, the maximum melt segregation of this last case is just larger than 15 %.

5.4 Transient evolution of the fault width h and of the segregation process

The progressive increase of melting with time $m(t)$ favours a progressive stiffening of the plastic slot in the deep crust. Stiffening ends with definitive locking of the plastic deformation. Assuming that the segregation process is uniform with depth, locking is expected to also be synchronous with depth. According to Equation 30, it occurs when the segregation rate m_s verifies:

$$\left(\frac{h}{h_{sc}}\right)^{-\frac{1}{3}} \times 10^{\left(\frac{m_s}{5\phi_{sc}} - 1\right)} \approx 4000 \quad (32a)$$

This rate is reached after a segregation time t_s of:

$$t_s = \frac{m_s}{\phi_0} \tau_s(h, \phi_0) \quad (32b)$$

In the above applications, t_s increases from 0.1 Ma to 60 Ma when h increases from 0.01 km to 10 km.

Eventually, if the shear presents a slow rate of expansion, the induced parabolic velocity profile in the fracture zone favours a progressive locking of the fault from the walls toward the axial region. Hence, the advance of the segregation process is likely to be inhomogeneous in time throughout the plastic slot. Assuming that the average time of locking inside the slot is still equal to t_s , the thinning velocity of the plastic slot $\frac{\partial h}{\partial t}$ verifies:

$$\frac{\partial h}{\partial t} = \frac{\phi_0 h_{sc}}{m_s \tau_s^{sc}} \left(\frac{\phi_0}{\phi_{sc}} \right) \quad (32c)$$

For the applications considered in Table 1, $\frac{\partial h}{\partial t}$ is about 0.15 mm/yr. Moreover, we assume that the upwelling flow balances the flow of the rigidified mush accreted along the walls of the shear zone throughout the whole crust thickness d_c ($d_c \approx 35$ km). This situation happens when the motion of the fault is about 0.15 mm/yr, and when the average upwelling velocity is $v_m = 0.15 \text{ mm/yr} \times d_c/h$. The mean upwelling flow velocity v_m decreases from 50 cm/yr to 0.5 mm/yr when h increases from .01 km to 10 km. During the segregation time t_s , the upwelling flow moves upwards by about 50 km; i.e. a value comparable to the thickness of the crust d_c . A rate of 0.15 mm/yr is a plausible value for a continental shear zone rate of expansion. All these elements indicate that melt can segregate within a plastic deforming shear zone of nearly constant thickness. Nevertheless, the upwelling flow also generates shear. Such stresses are important close to the walls and weak along the axis of the shear zone. Thus, a second segregation process may be generated close to the walls of the fault. In this situation the plane (σ_1, σ_2) makes an angle of 45° with the vertical. Thus veins should also take the same geometry.

6. Geological implications

Melting represents, along with shear, the main energetic response to orogenic processes [Burg, 1999]. It therefore appears obvious that both mechanisms should combine to segregate magma. Our model documents several points that reinforce field observations.

6.1 Magma generation as a combination of non linear interactions

Magma generation as a self organised interaction between melting and shear has already been suggested but not proven [Brown and Solar, 1998]. It would result from

nonlinear interactions and feedback loops. Several sources of non linearity were listed as melting, irregularly distributed in time and space, as well as the rheology that combines linear and non linear behaviours [Burg and Vigneresse, 2002]. On a more general ground, large scale interactions have been described between thrusting combined with shear and granitic magma emplacement [Brown and Solar, 1998]. Nevertheless, only a qualitative description has been issued in both cases, without demonstrating how these non linear effects interact.

Our model suggests solving two coupled non-linear equations in which instabilities develop. As in most non-linear systems, the final behaviour cannot be predicted from a simple inspection of the equations and **it** presents irregularities with time. Our model consequently profoundly differs from a continuous and regular extraction of the melt out of its matrix by single compaction [McKenzie, 1984], or from instabilities numerically induced [Brown et al., 1995]. In these models, the geometry of the initial perturbation triggers the solution. In contrast, two instabilities generated by different mechanisms cooperate in our model. One results from an upward obstruction to melt flow that favours vertical melt collection under compaction. At the same time, a second effect due to shear concentrates melt horizontally (Figure 3). Both instabilities develop with a wavelength close to the compaction length L that proves relatively stable when checked with the variation of remaining parameters.

The main contribution of our model concerns the estimation of the time needed to generate both non-linear instabilities (Equations 27 and 28). Because of the non-linear dependence of the matrix viscosity on the strain rate, the times for compaction and **for** channelling during shear are strongly dependent on the width of the shear zone. When the width of the shear zone is large, here 10 km, the compaction time is close to the time for shear, but it is so long that both instabilities are unlikely to develop in real fracture zones.

When the width of the shear zone is about 10 m to 100 m, the shear time reaches values ranging between 30 ka and 300 ka (Table 1). As a consequence, only veins sub-parallel to the (σ_1, σ_2) plane are generated. It is therefore inferred that the frequent occurrence of leucosome veins in migmatites likely result from such a channelling segregation process (Figure 1).

6.2 Discontinuous magma extraction with time

It is a direct consequence of the non-linear interactions generated by shear and compaction. Whereas the porosity waves concentrate and drive the melt vertically, the shear effect dries out all melt horizontally in the interval between two spikes. Deformation and melting consequently interact, which results in a discontinuous melt extraction process. This corresponds to observations **about** the chemical composition of the released melt [Sawyer, 1994]. When **the** melting **rate** is low compared to deformation, melt stays **longer** in contact with its matrix. It consequently has time to re-equilibrate with the matrix. Conversely, when the melt is rapidly extracted, it remains in chemical disequilibrium. Bursts in magma segregation have also been observed in numerical simulations [Vigneresse and Burg, 2000] and analogue models [Barraud et al., 2001; Bons et al., 2001]. Using a cellular automaton to describe melt extraction under deformation **results in** melt extraction by alternates bursts. The model, though stationary since it assumes an infinite source and sink for the melt, demonstrates that the quantity of extracted melt oscillates around an average value, mainly reflecting the initial amount of melt present in the system [Vigneresse and Burg, 2000]. However, pure and simple shear do not tend to a spatial organisation of melt extraction. Similar bursts of magma, represented by gas [Bons et al., 2001] or by molten paraffin in analogue models [Barraud et al., 2001], also show the discontinuous character of magma segregation. However this effect could not be quantified in analogue models. We are presently able to constrain time for melt extraction. As shown in Section 4, during the

runaway ending a segregation cycle, the growth of the channelling instability becomes exponential: i.e. the melt concentration in the spikes is multiplied by about 20, and the remaining interstitial melt concentration is divided by the same amount during a fraction of the time needed to perform a complete cycle (Figure 4). Hence, although each segregation cycle lasts between 30 ka to 300 ka, the final phase of the segregation process can be fast enough to explain the 10 ka melt extraction time of some Himalayan granites [Harris et al., 2000].

We provide insights on the processes that contribute to the discontinuous character of segregation. One is the rotation of the veins during shear. In section 5.2 we show that the veins, initially oriented parallel to the (σ_1, σ_2) plane, rotate towards the shear direction. As long as the veins remain clearly secant to the shear direction, strain locates inside the bulk of the mush. But when the veins and the shear are parallel, strain partitions into the veins and the segregation stops. A second reason for a discontinuous segregation results from the non linear evolution of the melt extraction velocity during segregation. For instance, at the end of a segregation pulse, when all the inter-granular melt has been expelled, the melt extraction is reactivated only after about 5 % of melt has been produced (see section 5.3). Melt production basically depends on the heating rate, the latter being driven essentially by heat diffusion if it gives place to continuous melting. It indirectly points to the time for heat to diffuse through the distance to the heat source (section 5.3). Our best estimate is when the heat source is not too far ($D \approx 10$ km) from the melting zone, then 5% of melt is produced in about 0.3 Ma. It is only after this period of time that the segregation process accelerates and quickly squeezes the remaining melt during the runaway. The last reason for discontinuous melt extraction is the stiffening of the matrix because of its dehydration (see section 5.2). As suggested in section 5.4, when the mush rises along the fault axis, clamping of plastic deformation starts along the limbs of the fault. Thereafter, the clamping front migrates inwards at a velocity of

0.075 mm/yr. In case of a fault moving at a full rate of 0.15 mm/yr, its plastic thickness remains steady. Otherwise, at any horizontal level, the plastic thickness of the fault increases or decreases with time. This triggers discontinuous modifications of the shear stress and thus also of the segregation process. All these facts suggest that the determination of the orientations and distances between veins in migmatite outcrops can be used to decipher the orientation of the (σ_1, σ_2) plane, the time of generation of the veins and the effective thickness of the plastic slot during melt segregation.

6.3 A narrow window for instabilities to develop and become stationary

Our model is also surprisingly well constrained numerically. We insist on the validity of these numbers. Owing to the large number and range of parameters, results should fit observations within the same order of magnitude. The compaction length should remain within a metric range (0.33-3.5 m). The compaction time should remain larger than shear channelling time, leading to vertical veins. Despite the large number of all parameters, a very few of them ultimately control instability development. In fact two parameter values need to be evaluated: the instantaneous thickness of the shear zone h and the distance D to the heating source. The values of both parameters are not independent because the couple of values h and D determines the bulk melt concentration during segregation ϕ_0 (Equation 31a). If $\phi_0 > 20\%$, the system blows up by loss of cohesion of the solid matrix; in contrast, if $\phi_0 < 5\%$, or $h \approx 10$ km, the segregation of melt is too sluggish to occur within an acceptable period of time. In table 1, the thickness of the plastic slot h likely ranges from 10 m up to 1 km. The distance of the heat source D that maintains an effective inter-granular melt concentration ϕ_0 of about 5 %, increases from 2.7 km to 27 km. Observations state crustal melts production at about 6-7 kbar (17-20 km in depth), that is about 12 km above the mantle where the hot source could generate heat. Therefore, our preferred value for D is about 10

km, implying also that our preferred thickness of the plastic slot h is about 100 m. This couple of values permits about 4 successive cycles of melt segregation before the matrix becomes too stiff to allow melt extraction (see Equation 30 and section 5.4). Thus in total about 20 % of melt can be extracted in about 1.2 Ma (Table 1). Outside those limits, the model either blows up or stops. Other scenarii are possible. For instance, some sequences of melt segregation with $h= 10$ m and $D= 2.7$ km can occur. In that case the maximum rate of melt segregation is 15 %, and melt is extracted in less than 90 ka.

These numbers fit field observations quite well. The compaction length observed in migmatites is metric in size (Figure 1). The time to extract melt fits those observed from isotope chemistry and thermochronometry [Harris et al., 2000]. The quantity of melt roughly matches the quantity of granitic magma (about 0.25) that can be generated from an amphibolitic rock to produce a granulitic restite (about 0.75) [Wedephol et al., 1991].

7. Conclusions

We have reviewed the different formulations of the equations for melt segregation and showed how they can be simplified to account for both compaction and shear. The method used to evaluate the shear stress terms is inspired by that developed by Stevenson [1989]. Manipulating with care Bercovici and Ricard [2003]'s basic equations for **two-phase** flow, we found that the driving term for melt channelling during shear is proportional to the stress due to shear $\mu_m c_0$. This shows that the development of channelling or localisation processes does not require a dependence on the matrix viscosity μ_m or on the surface stresses due to surface tension $\vec{\nabla}(\sigma\alpha)$ with melt concentration ϕ [Stevenson, 1989; Ricard et al., 2001]. Besides, we propose a set of simplifications giving a physically sound description of compaction and channelling with two independent sets of 1-D non-linearly coupled equations. Instabilities develop with associated wavelengths and they cooperate to segregate

melt. Compaction induces vertical areas in which porosity increases, thus enhancing vertical melt transport. Shear channels horizontal flow of melt in veins that rapidly absorb all the interstitial melt in between them. The instability wavelength increases with increasing melt content, as well as with the thickness of the shear zone. Because the crust is commonly stiff, shear channelling is much more efficient compared to compaction. The system of equations is calibrated against all varying parameters. We fixed them according to a crustal-derived magma generated from dehydration melting of an intermediate, amphibolitic crust. Surprisingly, only a few parameters control the times and lengths associated to the instabilities. When analysed in terms of time, they show that **granitic** melt channeling happen only within a very restricted window. The initial content of melt must be low. The amount of available melt ϕ_0 during each cycle is around 5%. Several cycles of melt extraction may develop successively, controlled by the possibility of melt to be extracted, but also to be generated. Indeed they fix the place where the molten layer may develop according to the position of the hot intrusion. The intrusion point may be located at the base of the crust, inducing melting in the intermediate crust, about 10 km above it. Successive melt extraction pulses occur, as has been observed in analogue and numerical models. They lead to a progressive stiffening of the matrix, which severely limits the number of cycles of extraction. We suggest a time for channelling of about 0.3 Ma, which implies that several pulses of magma can be generated within 1.2 Ma, before the matrix is clamped. This leads to a total of about 20 % of melt that can be extracted out of a typical source region.

The system of equations used to describe melt segregation is over-simplified and assumes equations of state that have not been completely proven. The validity of the results of the modelling thus requires confrontation with other models, for instance, those models in which the shear instability is generated by the matrix viscosity dependence on porosity or by the interfacial tension and a local damage. In these cases, the growth rate amplitude is

proportional to the solid viscosity variation with melt concentration or to the amplitude of surface tension, whereas in our model it is proportional to the shear stress amplitude. It remains that the growth rate of all the models varies with wave number k as $k^2/(1+k^2)$, (see Equation 19 and Stevenson, [1989] or Ricard et al, [2001]). Spiegelman, [2003] found the same behaviour for the stability analysis curve when the shear instability develops in a non-prescribed shear field and is thus coupled with melt segregation. Future work should consider the specific effects of interfacial tension, damage, and of the coupling between melt segregation flow S and shear flow C on the migration of granitic melts. Presently, many laboratory experiments study fluid migration during shear [Barraud et al., 2001, Holtzman et al., 2003, Schmocker et al., 2003]. Careful comparisons between numerical and laboratory results can help to validate the equations for two-phase flows. For instance, we hope that the true expression of the effective pressure equation of state (Equation 2a) which is equivalent to the determination of the true expression for the “bulk viscosity” can be deduced from a very precise comparison between laboratory and numerical experiments. However, the success of the crosscheck supposes to perfectly control the equation of state for the matrix rheology, the mush permeability and surface tension of the mush used in laboratory experiments. Now that the mathematical formalism to study melt segregation is almost complete, the proposed cross-check could be worthy.

Acknowledgments: This research was partly funded by the program Ecodev. It has also been initiated in the frame of GDR Transmet and ACI "Suspensions magmatiques". Constructive reviews by D.J. Stevenson, D. Bercovici and D. Komatitsch improved the manuscript.

References

- Agee, C.B. and Walker, D., Olivine flotation in mantle melt. *Earth Planet. Sci. Lett.*, **114**, 315-324, 1993.
- Barcilon, V. and Richter, F.M., Non-linear waves in compacting media. *J. Fluid Mech.*, **164**, 429-448, 1986.
- Barraud, J., Gardien, V., Allemand, P. and Grandjean, P., Analog modelling of melt segregation and migration during deformation. *Phys. Chem. Earth*, **A26**, 317-323, 2001.
- Bercovici, D., and Ricard, Y., Energetics of a two-phase model of lithospheric damage, shear localization and plate boundary formation, *Geophys. J. Int.*, 152, 581-596, 2003.
- Bercovici, D., Ricard, Y. and Schubert, G., A two phase model for compaction and damage, Part 1: General theory. *J. Geophys. Res.*, **B106**, 8887-8906, 2001a.
- Bercovici, D., Ricard, Y. and Schubert, G., A two-phase model for compaction and damage. Part 3. Application to shear localisation and plate boundary formation. *J. Geophys. Res.* **B106**, 8925-8939, 2001b.
- Bons, P.D., Dougherty-Page, J. and Elburg, M.A., Stepwise accumulation and ascent of magmas. *J. Metam. Geol.*, **19**, 627-633, 2001.
- Brown, M. and Solar, G.S., Shear-zone systems and melts: feedback relations and self-organization in orogenic belts. *J. Struct Geol.*, **20**, 211-227, 1998.
- Brown, M., Averkin, Y.K., McLellan, E.L and Sawyer, E., Melt segregation in migmatites. *J. Geophys. Res.*, **B100**, 15655-15679, 1995.
- Brown, M.A., Brown, M. Carlson, W.D. and Denison, C., Topology of syntectonic melt-flow networks in the deep crust: Inferences from three-dimensional images of leucosome geometry in migmatites. *Am. Min.*, **84**, 1793-1818, 1999.
- Burg, J.P. and Vigneresse, J.L., Non-linear feedback loops in the rheology of cooling-crystallising felsic magma and heating-melting felsic rock. In: de Meer, S., Drury, M., de

- Bresser, J.H. and Pennock, G., *Deformation Mechanisms, Rheology and Tectonics*. Geol. Soc. London Sp. Publ. **200**, 275-292, 2002.
- Burg, J.P., Ductile structures and instabilities: their implication for Variscan tectonics in the Ardennes. *Tectonophysics*, **309**, 1-25, 1999.
- Ceuleneer, G. and Rabinowicz, M., Mantle flow and melt migration beneath oceanic ridges: models derived from observations in ophiolites. In: Phipps Morgan, J., Blackman, D.K. and Sinton, J.M., (eds), *Mantle flow and melt generation at Mid-Ocean Ridges*. Am. Geophys. Union Mon. **71**, 123-154, 1992.
- Ceuleneer, G., Monnereau, M. and Amri, I., Thermal structure of a fossil mantle diapir inferred from the distribution of mafic cumulates. *Nature*, **379**, 149-153, 1996.
- Clemens, J.D., The granulite – granite connexion. In: Vielzeuf, D. and Vidal, P., (eds), *Granulite and crustal evolution*. Kluwer Acad. Publ., Dordrecht, NATO ASI series **C311**, 25-36, 1990.
- Drazin, P.G. and Johnson, R.S., *Solitons : an introduction*. Cambridge Univ. Press, Cambridge, 226p., 1989.
- Fontaine, F., Rabinowicz, M. and Boulegue, J., Hydrothermal Processes at Milos Island and the mechanisms of compaction-induced Phreatic Eruptions. *Earth Planet. Sci. Lett.*, **210**, 17-33, 2003.
- Harayama, S., Youngest exposed granitoid pluton on Earth: Cooling and rapid uplift of the Pliocene-Quaternary Takidani granodiorite in the Japan Alps. *Geology*, **20**, 657-660, 1992.
- Harris, N., Vance, D. and Ayres, M., From sediment to granites : timescales of anatexis in the upper crust. *Chem. Geol.*, **162**, 155-167, 2000.
- Hirth G. and Kohlstedt, D., Experimental constraints on the dynamics of the partially molten upper mantle: Deformation in the diffusion creep regime. *J. Geophys. Res.*, **B100**, 1981-2001, 1995.

- Holtz, F., Roux, J., Ohlhorst, S., Behrens, H. and Schulze, F., The effects of silica and water on the viscosity of quartzofeldspathic melts. *Am. Min.*, **84**, 27-36, 1999.
- Holtzman, B.K., Groebner, N.J., Zimmerman, M.E., Ginsberg, S.B. and Kohlstedt, D.L., Stress-driven melt segregation in partially molten rocks *Geochem., Geophys., Geosyst.*, **4**, doi:10.1029/2001GC000258, 2003.
- Kirby, S.H. and Kronenberg, A.K., Rheology of the lithosphere: Selected topics. *Rev. Geophys.*, **25**, 1219-1244, 1987.
- Laporte, D. and Provost, A., The grain-scale distribution of silicate, carbonate and metallosulfide partial melts : a review of theory and experiments. In : Bagdassarov, N., Laporte, D. and Thompson, A.B., (eds), *Physics and chemistry of partially molten rocks*. Kluwer Academic Press, Dordrecht, 93-140, 2000.
- Laporte, D., Wetting behaviour of partial melts during crustal anatexis: the distribution of hydrous silicic melts in polycrystalline aggregates of quartz. *Contrib. Min. Pet.*, **116**, 486-499, 1994.
- Lejeune, A.M. and Richet, P., Rheology of crystal-bearing silicate melts: an experimental study of high viscosities. *J. Geophys. Res.*, **B100**, 4215-4229, 1995.
- Leloup P.H., Arnaud, N., Lacassin, R., Kienast, J.R., Harisson, T.M., Phan Trong, T.T., Replumaz, A. and Tapponier, P., New constraints on the structure, thermochronology, and timing of Ailio Shan-Red River shear zone, SE Asia, *J. Geophys. Res.*, **B106**, 6683-6732, 2001.
- Maaloe, S. and Scheie, A., The permeability controlled accumulation of primary magma. *Contrib. Min. Pet.*, **81**, 350-357, 1982.
- McKenzie, D., The generation and compaction of partially molten rocks. *J. Petrol.*, **25**, 713-765, 1984.

- Mehnert, K.R., *Migmatites and the origin of granitic rocks*. Elsevier, Amsterdam, 393 p., 1968.
- Mehnert, K.R., Büsch, W. and Schneider, G., Initial melting at grain boundaries of quartz and feldspar in gneisses and granulites. *Neue J. Min. Mon.*, **4**, 165-183, 1973.
- Minarik, W.G. and Watson, E.B., Interconnectivity of carbonate melt at low melt fraction. . *Earth Planet. Sci. Lett.* , **133**, 423-437, 1995.
- Patiño Douce, A.E. and Johnston, A.D., Phase equilibria and melt productivity in the pelitic system: Implication for the origin of peraluminous granitoids and aluminous granulites. *Contrib. Min. Pet.*, **107**, 202-2183, 1991.
- Patiño Douce, A.E., What do experiments tell us about the relative contributions of crust and mantle to the origin of granitic magmas. In : Castro, A., Fernandez, C. and Vigneresse, J.L., (eds), *Understanding granites : Integrating new and classical techniques*. Geol. Soc. London Sp. Publ. **168**, 55-75, 1999.
- Petford, N., Cruden, A.R., McCaffrey, K.J.W. and Vigneresse, J.L., Granite magma formation, transport and emplacement of the Earth's crust. *Nature*, **408**, 669-673, 2000.
- Pichavant, M., Holtz, F. and McMillan, P., Phase relations and compositional dependence of water solubility in quartz-feldspar melts. *Chem. Geol.*, **96**, 303-319, 1992.
- Rabinowicz, M., Genthon, P., Ceuleneer G. and Hillairet, M., Compaction in a mantle mush with high melt concentrations and the generation of magma chambers. *Earth Planet. Sci. Lett.*, **188**, 313-328, 2001.
- Rabinowicz, M., Ricard, Y. and Grégoire, M., Compaction in a mantle with a very small melt concentration: Implications for the generation of carbonatitic and carbonate-bearing high alkaline mafic melt impregnations. *Earth Planet. Sci. Lett.*, **203**, 205-220, 2002.
- Renner, J., Evans, B. and Hirth, G., On the rheologically critical melt fraction. *Earth Planet. Sci. Let.*, **181**, 585-594, 2000.

- Ricard, Y., Bercovici, D. and Schubert, G., A two-phase model for compaction and damage. Part 2. Application to compaction, deformation, and the role of interfacial surface tension. *J. Geophys. Res.*, **B106**, 8907-8924, 2001.
- Richter, F.M. and McKenzie, D., Dynamical models for melt segregation from a deformable matrix. *J. Geol.*, **92**, 729-740, 1984.
- Rybacki, E. and Dresen, G., Dislocation and diffusion creep of synthetic anorthite aggregates. *J. Geophys. Res.*, **B105**, 26017-26036, 2000.
- Sawyer, E.W., Melt migration in the continental crust : distribution and movement of melt in anatectic rocks. *J. Metam. Geol.*, **19**, 291-30, 2001.
- Sawyer, E.W., Melt segregation in the continental crust. *Geology*, **22**, 1019-1022, 1994.
- Scaillet, B., Holtz, F. and Pichavant, M., Rheological properties of granitic magmas in their crystallization range. In: Bouchez, J.L., Hutton, D.H.W. and Stephens, W.E., (eds), *Granite: From Segregation of Melt to Emplacement Fabrics*. Kluwer Acad. Publ., Dordrecht, 11-31, 1997.
- Schmocker M., Bystricky, M., Kunze, K., Burlini, L., Stunitz, H. and Burg, J.P., Granular flow and Riedel band formation in water-rich quartz aggregates experimentally deformed in torsion, *J. Geophys. Res.*, **B108**, 2242, doi:10.1029/2002JB001958, 2003.
- Scholz, C.H., *The mechanics of earthquakes and faulting*. Cambridge Univ. Press, New York, 439 p., 1990.
- Scott, D. and Stevenson, D., Magma ascent by porous flow. *J. Geophys. Res.*, **B91**, 9283-9296, 1986.
- Scott, D. and Stevenson, D., Magma solitons. *Geophys. Res. Lett.*, **11**, 1161-1164, 1984.
- Scott, D., The competition between percolation and circulation in a deformable porous rock. *J. Geophys. Res.*, **B93**, 6451-6462, 1989.

- Sleep, N.H., Segregation of magma from a mostly crystalline mush. *Geol. Soc. Am. Bull.*, **85**, 1225-1232, 1978.
- Spiegelman, M., Linear analysis of melt band formation by simple shear (Submitted *Geochem., Geophys., Geosys.*, 4, 9, 8615, 10.1029/2002GC000499, 2003.
- Stevenson, D.J., Spontaneous small scale melt segregation in partial melts undergoing deformation. *Geophys. Res. Lett.*, **16**, 1067-1070, 1989.
- Sumita, I.S., Yoshida, S., Kumazawa, M. and Hamano, Y., A model for sedimentary compaction of a viscous medium and its application to inner core growth. *Geophys. J. Int.*, **124**, 502-524, 1996.
- Thompson, A.B., Dehydration melting of pelitic rocks and the generation of H₂O-undersaturated granitic liquids. *Am. J. Sci.*, **282**, 1567-1595, 1982.
- Vasiliev, O.V., Podladchikov, Y.Y. and Yuen, D.A., Modeling of compaction driven flow in poro-viscoelastic medium using adaptive wavelet collocation method. *Geophys. Res. Lett.*, **25**, 3239-3242, 1998.
- Vigneresse, J.L. and Burg, J.P., Strain rate dependent rheology of partially molten rocks. In: Vertical and Horizontal Decoupling in the Lithosphere. In: Grocott, J., McCaffrey, K.J.W., Taylor, G. & Tikoff, B. (eds) *Vertical and Horizontal Decoupling in the Lithosphere*. Geolo. Soc. London, Sp. Publ., (in press) 2003.
- Vigneresse, J.L. and Burg, J.P., Stable continuous versus discontinuous melt segregation in migmatites. *Terra Nova*, **12**, 188-192, 2000.
- Vigneresse, J.L., Barbey, P. and Cuney, M., Rheological transitions during partial melting and crystallisation with application to felsic magma segregation and transfer. *J. Petrol.*, **37**, 1579-1600, 1996.

Wedepohl, K.H., Heinrichs, H. and Bridgewater, D., Chemical characteristics and genesis of the quartz-feldspathic rocks in the Archean crust of Greenland. *Contrib. Min. Pet.*, **107**, 163-179, 1991.

Wiggins, C. and Spiegelman, M., Magma migration and magmatic solitary waves in 3-D. *Geophys. Res. Let.*, **22**, 1289-1292, 1995.

Wilks, K.R. and Carter, N.L., Rheology of some continental lower crustal rocks. *Tectonophysics*, **182**, 57-77, 1990.

Table 1

h (km)	D (km)	m (%)	μ_l (Pa.s)	μ_m (Pa.s)	c_0 (s ⁻¹)	SH (MPa)	L (m)	τ_c (Ma)	τ_s (Ma)	δl (km)
.01	2.7	5	10^4	$2.2 \cdot 10^{15}$	10^{-10}	.22	.33	2.6	.03	0.6
		10	10^5	$2.2 \cdot 10^{16}$		2.2		26		
		15	10^6	$2.2 \cdot 10^{17}$		22		260		
		20	10^7	$2.2 \cdot 10^{18}$		220		2600		
.1	8.7	5	10^4	10^{16}	10^{-11}	.1	0.73	5.7	0.3	5.4
		10	10^5	10^{17}		1		57		
		15	10^6	10^{18}		10		570		
		20	10^7	10^{19}		100		5700		
1	27	5	10^4	$4.6 \cdot 10^{16}$	10^{-12}	.046	1.6	12	3	54
		10	10^5	$4.6 \cdot 10^{17}$.46		120		
		15	10^6	$4.6 \cdot 10^{18}$		4.6		1200		
		20	10^7	$4.6 \cdot 10^{19}$		46				
10	43	10	10^4	10^{17}	10^{-13}	.01	3.5	20	15	270
		20	10^6	10^{19}		1		2000		
		30	10^8	10^{21}		10				

Table 1. Parameter values for three distinct channelling experiments: the thickness of the fault zone h , the distance between the heat source and the melting zone D , the shear strain c_0 , the total melting proportion m , the liquid and solid viscosities $\mu_l(m)$ and $\mu_m(m, c_{sc})$, the shear stress $SH = c_0\mu_m$, the compaction length L , the channelling time τ_s , the compaction time τ_c and the horizontal displacement of the fault during δl . Values are given at the beginning of each segregation loop.

Figure captions

Figure 1 Picture of a migmatitic rock in Curais Novos, Brazil. The scale is approximately two meters horizontally. Clear veins of melt, or leucosomes, segregate under a dextral shear, within a non yet totally molten matrix.

Figure 2 Viscosity values according to H₂O content in a peraluminous magma.

Figure 3 Geometry of melt segregation in a horizontal section of a shear zone, under stress field $C(x)$. The horizontal y-axis designates the shear direction, the x-axis the direction normal to the fault, of thickness h. The shear velocity along each limbs of the fault is $V/2$ and $-V/2$, respectively. The X-axis coincide with the direction of maximum stretching σ_3 and the Y-axis the direction of maximum compression σ_1 . In section 4, we show that the melt channelling occurs in the stretching direction σ_3 , along the X-direction. Melt accumulates in veins sub-parallel to the direction of maximum compression σ_1 , with a characteristic distance equal to the compaction length L. Straight lines T parallel to the Y-direction are thus those veins. In section 5.2, we show that the horizontal shear deforms the T lines in S-shape lines.

Figure 4 Snapshots of the porosity profiles for our reference model. The numerical experiment initiates with a sinusoidal profile (Equation 18) with the initial amplitude $\epsilon_0 = 0.2$ and the wavelength $\lambda_0 = 0.625$. 4a) Porosity profiles at time $t = 0, 0.5$ and 1 , respectively. Those profiles are undistinguishable to those deduced from the linear stability analysis (Equation 19); 4b - 2f) Porosity profiles at the respective time of $1.5, 2, 2.25, 2.35$ and 2.5 . The initial porosity distribution is drawn on the different figures to scale the evolution of the amplitude of porosity with time. Runaway starts when $t > 2$.

Figure 5 Models displaying a localized instability. The initial profiles initiate according to Equation 21. 5a - 5b) The local maxima of the initial porosity profiles are close ($A = 4$, $H = 5$ in Equation 21). Porosity profile are shown at time $t = 2$, and $t = 2.2$ respectively. Figures show an uniform segregation of the melt to build the melt peak at the top of the initial profile. 5c) The initial profile has very distant local maxima ($A = 40$ $H = 50$ in Equation 21). Snapshot at time $t = 2$ shows that the tear instability develops only with the melt available in its neighbourhood. A local minima initiates at a few compaction length from the maxima of the porosity wave.

Figure 6 Competition of instabilities with different wavelength. Experiments initiate with the porosity profile of Equation 22 in which two sinusoidal perturbations compete, each with a different wavelength λ_1 and λ_2 . The following wavelets couples of wavelets are used. 6a) $\lambda_1 = 5$, $\lambda_2 = 0.625$, 6b) $\lambda_1 = 5$, $\lambda_2 = 2.5$, $\lambda_2 = 0.625$; 6c) $\lambda_1 = 1.25$, $\lambda_2 = 0.625$; 6d) $\lambda_1 = 0.625$, $\lambda_2 = 0.3125$ respectively. Each figure displays the porosity snapshots at $t = 2$. Wavelets with $\lambda_1 \approx 1$ drain the essential part of the available melt.

Figure 7 Compaction experiments with a different obstruction (Equations 23), with snapshots at the time $t = 50$. 7a) The initial profile presents a weak obstruction ($c_\infty = 0.5$). 7b) the obstruction is drastic ($c_\infty = 0.001$). The generated melt pocket concentrates much more melt and are smaller when the experiment starts with a drastic obstruction.

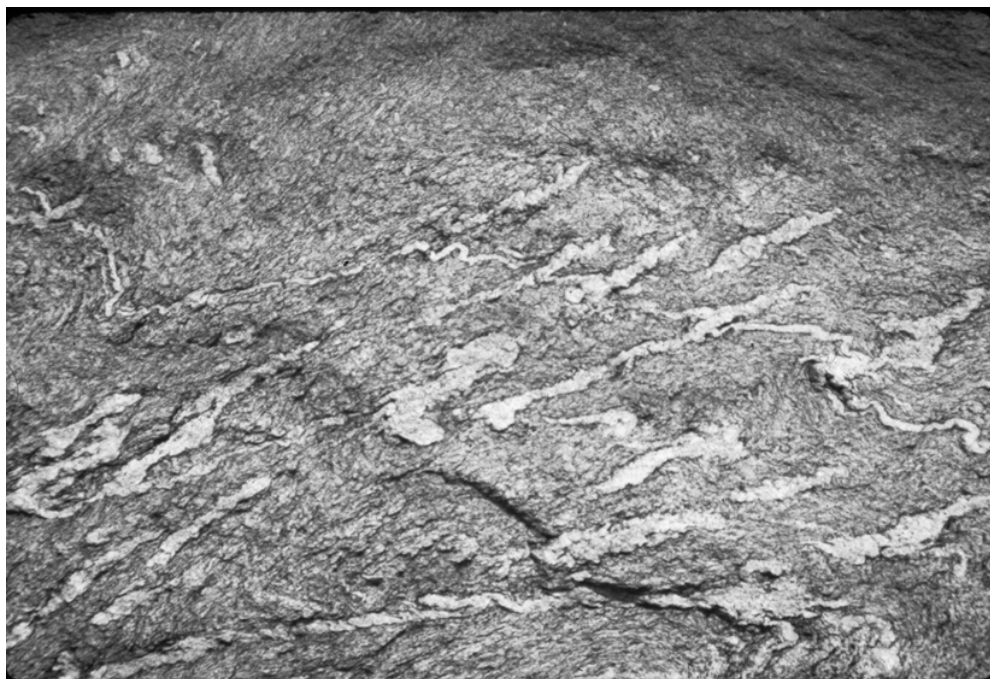
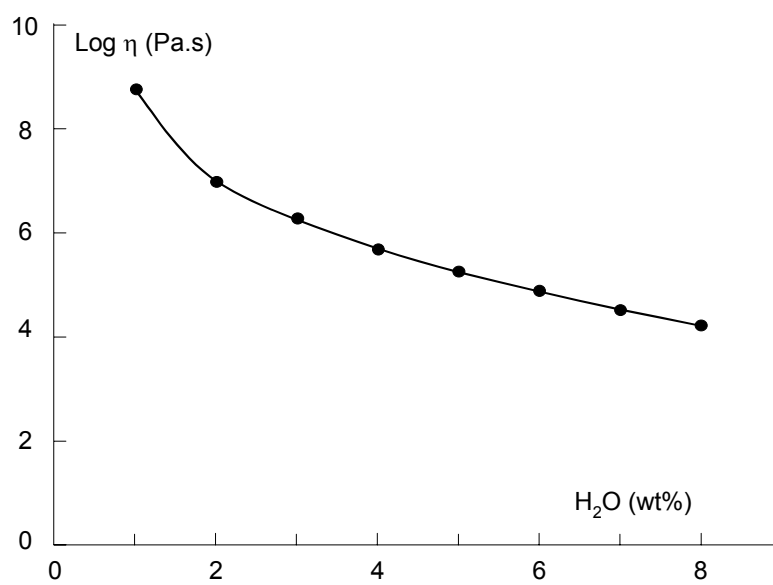


Figure 1

**Figure 2**

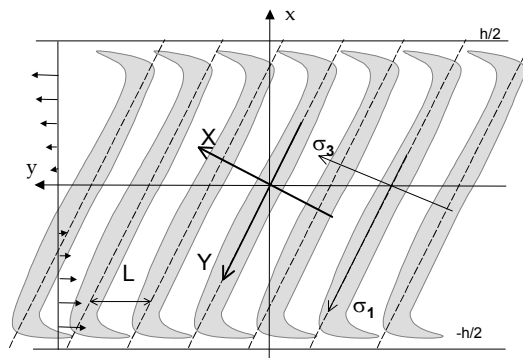
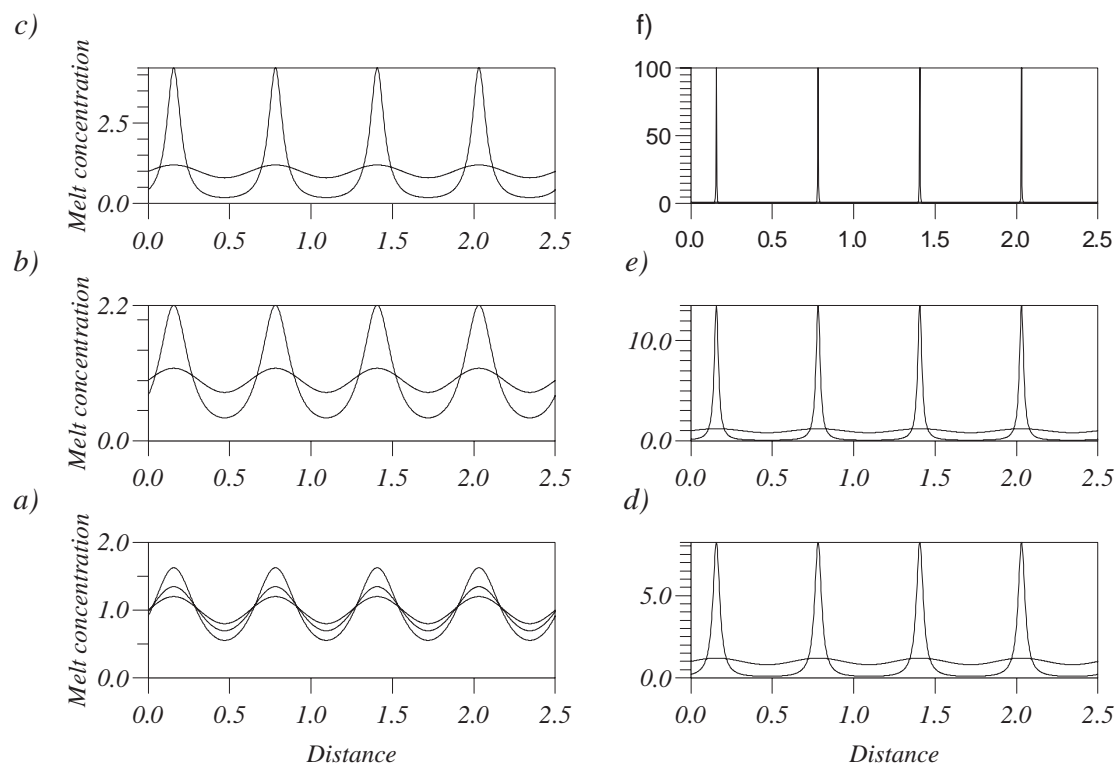
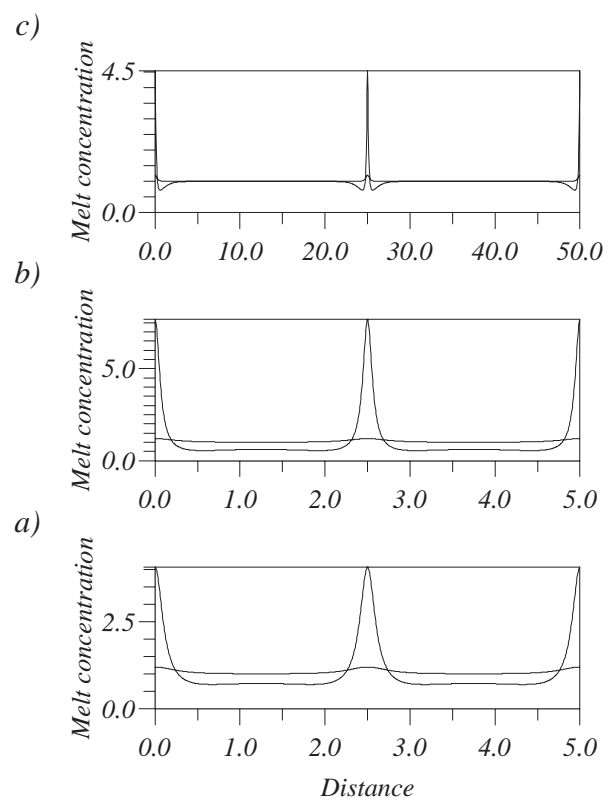
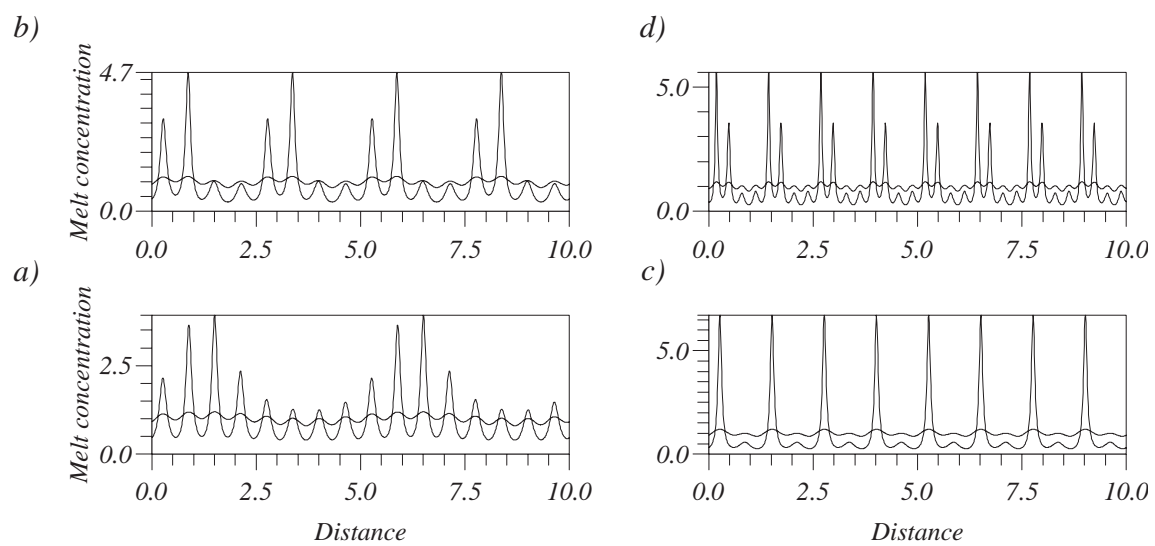


Figure 3

**Figure 4**

**Figure 5**

**Figure 6**

